

# 1 Global NO<sub>2</sub> Changes Between 2019 and 2024 as Observed by 2 TROPOMI in Urban Areas and Emerging Hotspots

3 Daniel E. Huber<sup>1</sup>, Gaige H. Kerr<sup>1</sup>, M. Omar Nawaz<sup>2</sup>, Sara Runkel<sup>3</sup>, Susan C. Anenberg<sup>1</sup>, Daniel L.  
4 Goldberg<sup>1</sup>

5 <sup>1</sup>Department Environmental and Occupational Health, Milken Institute School of Public Health, George Washington  
6 University, Washington, DC, USA

7 <sup>2</sup>School of Earth and Environmental Science, Cardiff University, Cardiff, United Kingdom

8 <sup>3</sup>National Center for Atmospheric Research, Boulder, CO, USA

9 *Correspondence to:* Daniel E. Huber (daniel.huber@gwu.edu)

10 **Abstract.** We present a global assessment of space-based urban nitrogen dioxide (NO<sub>2</sub>) observations from 2019 to 2024 using  
11 annual and monthly mean tropospheric vertical column densities (VCDs) from the TROPOspheric Monitoring Instrument  
12 (TROPOMI). Across 11,500 cities defined by the Global Human Settlement Layer-Settlement Model (GHS-SMOD), we find  
13 population-weighted annual mean urban NO<sub>2</sub> VCDs were lower in 2024 than 2019 in Europe (-13%) and Asia and Oceania (-  
14 17%), with seasonal decomposition indicating that annual changes are largely driven by concentration decreases during  
15 November-March. Aggregated urban VCD changes in North America, South America and Africa were statistically  
16 insignificant, though numerous individual cities exhibited significant changes. Of larger cities, Tehran had the largest annual  
17 mean NO<sub>2</sub> VCD ( $>30 \times 10^{15}$  molecules cm<sup>-2</sup>) and Seoul experienced the largest reduction ( $-9.4 \pm 1.0\%$  yr<sup>-1</sup>;  $p < 0.001$ ). We then  
18 calculate NO<sub>2</sub> VCD urban enhancements (VCD<sub>ENH</sub>) by removing background concentrations from urban signatures and  
19 compare VCD<sub>ENH</sub> to changes in nitrogen oxide (NO<sub>x</sub>) emissions from two emissions inventories, highlighting regions with  
20 potential inventory discrepancies. We find VCD<sub>ENH</sub> changes exceed changes in inventory NO<sub>x</sub> emissions in Europe, North  
21 America and Asia and Oceania, with worse agreement in the Global South. We further identify changes in NO<sub>2</sub> near fossil fuel  
22 operations and note conflict-related changes in NO<sub>2</sub>, highlighting the responsiveness of satellite NO<sub>2</sub> to certain societal  
23 disruptions. This work demonstrates the value in space-based remote sensing being an accountability agent for air pollution  
24 emissions on a global scale and to identify changes in NO<sub>2</sub> in otherwise unmonitored regions.

## 25 1 Introduction

26 Nitrogen dioxide (NO<sub>2</sub>) is a harmful air pollutant that originates from both anthropogenic and natural emissions sources,  
27 including fossil fuel combustion, biomass burning, lightning, and soils (Dix et al., 2020; Jin et al., 2021; Schuman & Huntrieser,  
28 2007; Huber et al., 2024), with fossil fuel combustion accounting for ~45% of total global nitrogen oxide emissions (Song et  
29 al., 2021). Only a small amount of NO<sub>2</sub> is emitted from these sources directly, with nitric oxide (NO) being the primary  
30 emissions product that quickly cycles to NO<sub>2</sub> in the presence of oxidants such as ozone (O<sub>3</sub>) or peroxy radicals (HO<sub>2</sub> or RO<sub>2</sub>).

31 The summed concentrations of NO and NO<sub>2</sub> are referred to as nitrogen oxides (NO<sub>x</sub> = NO + NO<sub>2</sub>), as the concentrations of  
32 NO and NO<sub>2</sub> are inherently linked. NO<sub>2</sub> is more commonly targeted by regulatory measures than NO, as it constitutes the  
33 majority of atmospheric NO<sub>x</sub> concentrations and is linked to increased morbidity and mortality from long-term exposure,  
34 particularly within urban environments (Chen et al., 2024). While NO<sub>x</sub> is commonly associated with health risks, the direct  
35 association between NO<sub>x</sub> exposure and adverse health outcomes remains uncertain (Anenberg et al., 2022). Despite this, NO<sub>x</sub>  
36 contributes to known harmful secondary pollutants, including O<sub>3</sub> and fine particulate matter.

37 NO<sub>2</sub> concentrations are measured using: (1) in-situ monitoring, e.g. chemiluminescence analyzers at the surface, or (2) remote  
38 sensing instrumentation leveraging the unique spectral properties of NO<sub>2</sub>, that absorbs light most efficiently in the visible  
39 portions (405 – 465 nm) of the electromagnetic spectrum (Lamsal et al., 2015). The latter method relies upon spectrometers  
40 detecting in the UV-Visible spectral range to infer NO<sub>2</sub> vertical column densities (VCDs), defined as the summed concentration  
41 of NO<sub>2</sub> in a column from the surface to an upper limit of the atmosphere, with the tropopause often used as the upper limit.  
42 Spectrometers have been used to measure NO<sub>2</sub> VCDs from ground-level directed upward, from aircraft directed downward, or  
43 from space-based satellites directed downward, including from the TROPOspheric Monitoring Instrument (TROPOMI)  
44 onboard the Sentinel-5P satellite (Herman et al., 2009; Fishman et al., 2012; Veeffkind et al., 2012). NO<sub>2</sub> can also be remotely  
45 sensed from ground-based instruments capable of inferring vertical profiles of NO<sub>2</sub>, such as using multi-axis differential optical  
46 absorption spectroscopy (MAX-DOAS; Vlemmix et al., 2010).

47 The earliest space-based spectrometers detecting NO<sub>2</sub> were flown on low-earth polar orbiting satellites and were launched  
48 within the mid-1990s to mid-2000s. These include the Global Ozone Monitoring Experiment (GOME; Burrows et al., 1999)  
49 and GOME-2 satellites, the SCanning Imaging Absorption spectroMETER for Atmospheric CHartography (SCIAMACHY;  
50 Bovensmann et al., 1999) and the Ozone Monitoring Instrument (OMI; Levelt et al., 2006). The data collected using these  
51 instruments provided unique insight into atmospheric chemistry and composition across the globe, including in mostly  
52 unmonitored regions. OMI, launched in 2004, provided NO<sub>2</sub> VCDs at a spatial resolution of 13 × 24 km<sup>2</sup> at nadir and has  
53 remained operable for more than two decades at the time this was written, providing a valuable long-term record of NO<sub>2</sub>  
54 globally. OMI remained the highest resolution space-based NO<sub>2</sub> product until TROPOMI launched in 2017, which ultimately  
55 provided NO<sub>2</sub> VCDs at a spatial resolution of 3.5 × 5.5 km<sup>2</sup> at nadir. Observations at this resolution facilitated the evaluation  
56 of satellite NO<sub>2</sub> at previously unprecedented spatial scales, including at the intra-urban level (Goldberg et al., 2021; Goldberg  
57 et al., 2024).

58 NO<sub>2</sub> trends have been characterized in urban and broader environments using space-based instruments. Earlier satellite studies  
59 used the GOME and SCIAMACHY satellites to identify increasing NO<sub>2</sub> VCD trends in China from the mid-1990s to the mid-  
60 2000s (Richter et al., 2005; Stavrakou et al., 2008; Van der A et al., 2008), driven primarily by economic growth and  
61 industrialization. Later studies, incorporating OMI observations, highlighted further increases in China through the early  
62 2010s, with VCDs and satellite-inferred surface concentrations steadily declining since (Miyazaki et al., 2017; Wang et al.,  
63 2019; Jiang et al., 2022). Europe has exhibited steady NO<sub>2</sub> VCD declines since the start of the satellite NO<sub>2</sub> record (Richter et

64 al., 2005; Krotkov et al., 2016; Duncan et al., 2016), driven largely by the implementation of various emissions control  
65 technologies. In the United States, NO<sub>2</sub> concentrations generally exhibited a decreasing trend from 2005 through the mid-  
66 2010s (Lamsal et al., 2015), with VCD decreases more gradual since, in part due to an increased influence from regional  
67 background NO<sub>2</sub> levels (Jiang et al., 2018; Goldberg et al., 2021; Dang et al., 2023). In contrast, urban regions of India have  
68 shown NO<sub>2</sub> increases over the past few decades, linked to urbanization and energy demand growth (Hilboll et al., 2013; Ghude  
69 et al., 2020). Over Africa and South America, NO<sub>2</sub> VCD trends through the mid-2010s have been less pronounced, reflecting  
70 limited industrialization and more dominant contributions from biomass burning and natural sources (Geddes et al., 2016;  
71 Castellanos et al., 2014). Additionally, numerous studies have highlighted the influence that the COVID-19 pandemic had on  
72 NO<sub>2</sub> globally, with most regions globally exhibiting broad NO<sub>2</sub> decreases in 2020 during numerous lockdowns and subsequent,  
73 regionally-distinct rebounds in emissions (Lonsdale et al., 2023; Fisher et al., 2024).

74 Satellite studies have been used to characterize trends within the urban environment specifically, using different methods to  
75 characterize the urban extent. Geddes et al. (2016) used GOME, SCIAMACHY and GOME-2 oversampled to a  $0.1^\circ \times 0.1^\circ$   
76 grid to highlight NO<sub>2</sub> VCD trends globally, as well as in select urban areas, with the urban region defined as the surrounding  
77  $\sim 200 \text{ km} \times 200 \text{ km}$ . Fioletov et al. (2022) and Fioletov et al. (2025) used urban density from the Gridded Population of the  
78 World (SEDAC, 2017) as a proxy for the extent of the urban environment to identify changes in urban NO<sub>x</sub> emissions.  
79 Anenberg et al. (2022) used urban boundaries provided from the 2019 version of the Global Human Settlement Layer-  
80 Settlement model (GHS-SMOD) to evaluate NO<sub>2</sub> trends from 2000 – 2019 using surface NO<sub>2</sub> estimates derived from OMI  
81 NO<sub>2</sub> and a land-use regression model.

82 Here, we use TROPOMI tropospheric NO<sub>2</sub> VCDs to quantify general NO<sub>2</sub> changes globally from 2019 to 2024, with a  
83 particular focus on urban areas. The urban boundaries are defined by the 2023 version of GHS-SMOD, which provides urban  
84 cluster boundaries for all urban regions globally. We evaluate changes in annual mean urban NO<sub>2</sub> VCDs against NO<sub>x</sub> emissions  
85 inventories and characterize the influence of different seasons on annual variations. We additionally note changes in select oil,  
86 gas, and other mining regions, which exhibit the largest changes globally outside of urban areas. This study represents the first  
87 detailed global-scale analysis of urban TROPOMI NO<sub>2</sub> from 2019 to 2024. Our findings illustrate how NO<sub>2</sub> responded to  
88 specific societal events during this timeframe, such as the impact of clean air policies, population migration away from urban  
89 areas due to war, the increased demand for fossil fuels and rare-Earth minerals, and the emergence and waning of a global  
90 pandemic. Furthermore, by directly linking observed NO<sub>2</sub> urban enhancements with NO<sub>x</sub> emission inventory data from the  
91 updated EDGARv8.1, our work provides valuable insights into regions where emissions inventories align closely with  
92 observations, as well as areas exhibiting potential inventory discrepancies. This work underscores the critical value of satellite-  
93 derived NO<sub>2</sub> as a tool for urban air quality assessment and emissions management.

## 94 **2 Data and Methods**

### 95 **2.1 Global Human Settlement Layer Urban Cluster Boundaries**

96 The Global Human Settlement Layer-Settlement Model (GHS-SMOD; Schiavina et al., 2023) is a dataset developed by the  
97 Joint Research Centre of the European Commission containing spatial boundaries and population estimates for all urban areas  
98 globally with a population of at least 50,000, which can be used to subset gridded or spatially-disaggregated data for any built-  
99 up area on Earth. GHS-SMOD uses satellite remote sensing to identify the spatial extent and boundaries of all cohesive built-  
100 up areas globally at a spatial resolution of  $1 \times 1 \text{ km}^2$ , with each separate, cohesive built-up area referred to as an “urban cluster”.  
101 In this study, we use the terms “urban cluster” and “city” interchangeably, although we note that GHS-SMOD urban clusters  
102 do not always align with administrative city boundaries. GHS-SMOD has the benefit of providing a globally consistent,  
103 satellite-derived definition of built-up areas, whereas administrative boundaries vary widely in definition and availability.  
104 Using physical built-up area boundaries from GHS-SMOD instead of administrative ones may shift the absolute spatial extent  
105 of some cities, but it does not materially alter the concentrations calculated in this study.

106 The 2023 version of GHS-SMOD provides boundaries for approximately 11,500 urban clusters, along with population  
107 estimates for the year 2020 (Fig. S8). We note that GHS-SMOD urban clusters do not reflect the traditional boundaries of  
108 individual cities as we may understand them, and as such, GHS-SMOD urban clusters can span multiple cities, regions or even  
109 countries. For example, the urban cluster encompassing San Diego, California includes the city of San Diego, but also the  
110 adjacent surrounding suburbs, as well as the entirety of Tijuana, Mexico (Fig. S9). In such cases, attribution of an urban cluster  
111 to one particular city is not possible.

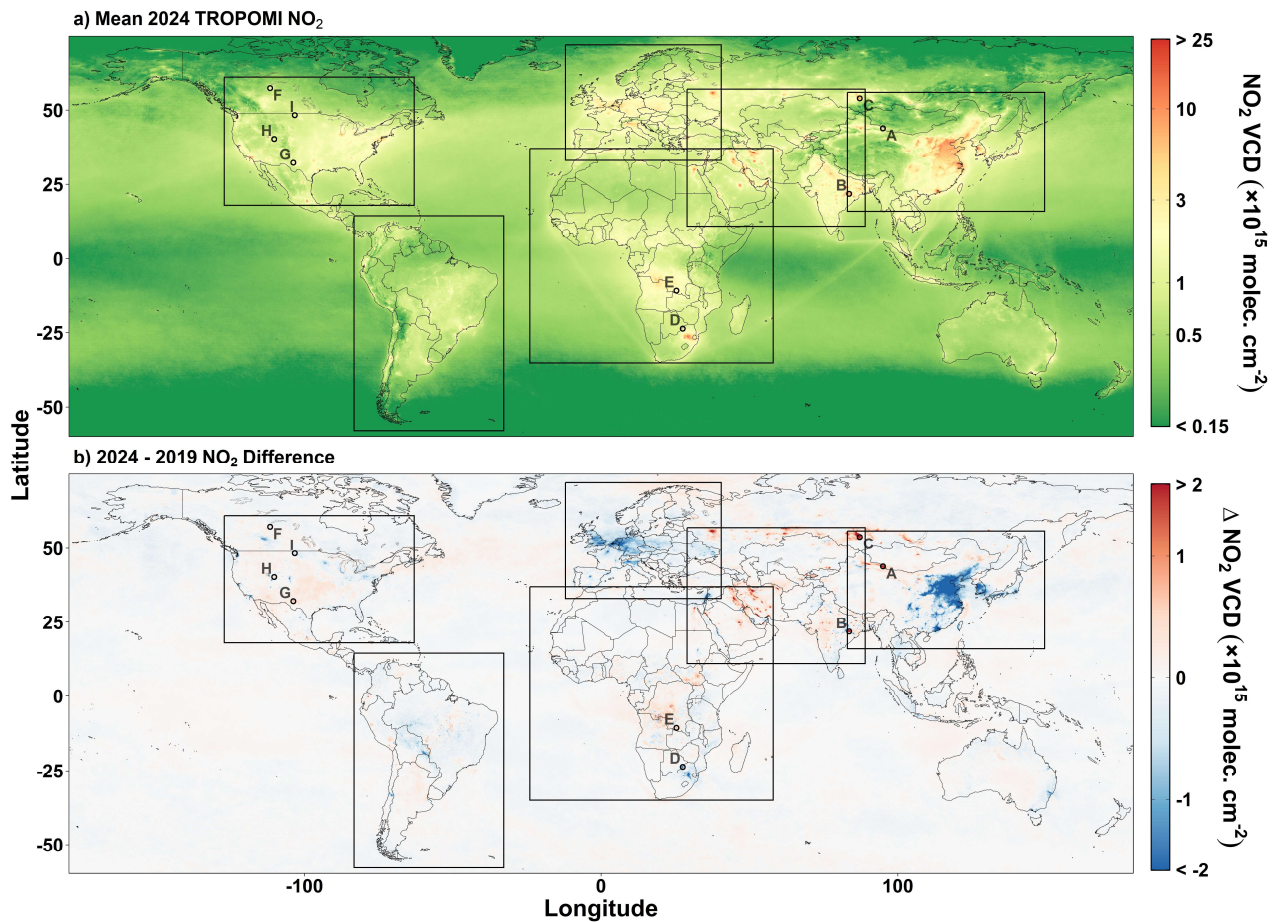
112 We use the GHS-SMOD boundaries to subset monthly- and annually-averaged satellite  $\text{NO}_2$  column concentration data for all  
113 urban clusters, as described in Section 2.2.1.

### 114 **2.2 TROPOMI $\text{NO}_2$ Vertical Column Densities**

115 The TROPOspheric Monitoring Instrument (TROPOMI) is a pushbroom spectrometer on board the Sentinel-5P satellite  
116 traveling in low earth orbit, with approximately one overpass each afternoon (Veefkind et al., 2012). Launched in October  
117 2017, TROPOMI detects radiation in spectral bands ranging from the ultraviolet to shortwave infrared to infer concentrations  
118 of various atmospheric constituents, including nitrogen dioxide ( $\text{NO}_2$ ), which is best inferred from the near-UV and visible  
119 portions of the spectrum. We use Level 3 monthly- and annually-averaged TROPOMI tropospheric  $\text{NO}_2$  vertical column  
120 densities (VCDs) on a  $0.1^\circ$  global grid (Goldberg, 2024), which were created by oversampling daily Level 2 TROPOMI  $\text{NO}_2$   
121 VCDs derived from version 2.4+ of the European Space Agency retrieval algorithm (van Geffen et al., 2022). These Level 2  
122 data have a nadir spatial resolution of  $3.5 \times 7.0 \text{ km}^2$  before and  $3.5 \times 5.5 \text{ km}^2$  after August 06, 2019. Data were quality  
123 controlled to remove Level 2 pixels with a  $qa\_value < 0.75$  before oversampling, which removes data with quality issues  
124 related to clouds, surface reflectivity (e.g. snow and ice) or other retrieval errors. The TROPOMI  $\text{NO}_2$  data used in this study

125 span six full calendar years from January 2019 to December 2024 (Fig. 1); we use the RPRO version from 1 January 2019 –  
126 25 July 2022 and the OFFL version from 26 July 2022 – 31 December 2024. On 7 September 2024 there was an update of the  
127 surface reflectivity assumptions and on 16 November 2024 there was an update to the cloud retrieval, both of which induce a  
128 small positive step change in the data but likely does not meaningfully affect the 2024 annual average.

129 TROPOMI NO<sub>2</sub> retrievals are subject to measurement and retrieval uncertainties that propagate into the oversampled Level 3  
130 products. Typical uncertainties in monthly or annually averaged tropospheric NO<sub>2</sub> vertical column densities are on the order  
131 of 15–20 %. Systematic biases have also been reported, with overestimation in less polluted regions (+26.5% bias) and  
132 underestimation in areas with high NO<sub>2</sub> concentrations (-31.4% bias), reflecting limitations in the retrieval process (Glissenaar  
133 et al., 2025; Lambert et al., 2025).



134  
135 **Figure 1: (a) Global 2024 annual average NO<sub>2</sub> VCDs colored on a log-scale and (b) the difference in VCD from 2019 to 2024 colored**  
136 **on a symmetric log-scale. Points labeled A-I correspond with locations of oil, gas and mining operations highlighted in Fig. 12. Boxes**  
137 **indicate select focus regions in Section 5.**

### 138 2.3 Quantifying Average TROPOMI NO<sub>2</sub> VCDs for GHS-SMOD Urban Clusters

139 For each urban cluster, we subset the oversampled TROPOMI data for grid cells that are located within 0.1° of the urban  
140 cluster boundary. For most cities, this results in approximately 20-25 grid cells, depending on the extent of the individual  
141 cluster. Given that the spatial resolution of GHS-SMOD is roughly an order of magnitude finer than that of the oversampled  
142 TROPOMI data (1 km vs. 0.1°) we interpolate the subsetted TROPOMI data to the 0.01° × 0.01° resolution of GHS-SMOD  
143 using a nearest neighbor approach. We then calculate an area-weighted average of interpolated grid cells that have a grid cell  
144 center falling within the urban cluster boundary (Fig. S9). This approach allows for the portions of oversampled 0.1° × 0.1°  
145 grid cells that may not be centered within an urban cluster boundary, but that still overlap with a cluster, to be accounted for  
146 within the average NO<sub>2</sub> column estimate.

147 To evaluate the changes in VCDs for broader regions, e.g. countries containing multiple urban clusters, we can calculate a  
148 population-weighted average VCD, taking into account varying population sizes in different urban clusters.

$$149 \quad VCD_{PW} = \frac{\sum_i(POP_i \times VCD_i)}{\sum_i(POP_i)}, \quad (1)$$

150 In Eq. 1, VCD<sub>PW</sub> represents the population-weighted VCD for a given country, POP<sub>*i*</sub> represents the 2020 GHS-SMOD-  
151 estimated population for a given urban cluster *i*, and VCD<sub>*i*</sub> represents the mean NO<sub>2</sub> VCD for *i*.

152 For each time series, we use monthly TROPOMI NO<sub>2</sub> columns from 2019–2024 to estimate a change in % yr<sup>-1</sup>. We first  
153 construct a de-seasonalized anomaly series by computing, for each calendar month at each location, the mean NO<sub>2</sub> over the  
154 full period and expressing each monthly value as a percent deviation from its corresponding monthly mean. To obtain the  
155 percent change per year and its standard error, we fit a linear regression to the original monthly series with time as the predictor  
156 and fixed effects for calendar month to control for seasonality. The estimated annual percent change and its standard error  
157 were taken directly from the time-slope coefficient and its standard error from this regression. To assess statistical significance,  
158 we regressed the de-seasonalized percent anomalies on time and obtained a p-value for the slope using standard errors that  
159 account for temporal autocorrelation.

### 160 2.4 Accounting for Background NO<sub>2</sub>

161 To account for changes in upwind background NO<sub>2</sub> concentrations that may influence urban NO<sub>2</sub> VCDs, we quantify an urban  
162 NO<sub>2</sub> enhancement.

$$163 \quad VCD_{ENH} = VCD_{UC} - VCD_{BG}, \quad (2)$$

164 In Eq. 2, VCD<sub>ENH</sub> is the urban NO<sub>2</sub> VCD enhancement, VCD<sub>UC</sub> is the NO<sub>2</sub> VCD within each urban cluster as described in  
165 Section 2.2.1, and VCD<sub>BG</sub> is the background concentration for an urban cluster. We define VCD<sub>BG</sub> for a given year as the 50<sup>th</sup>  
166 percentile of annual mean NO<sub>2</sub> VCDs extending 0.5 degrees in any direction from an urban cluster boundary. Previous studies

167 have used a percentile threshold to determine background concentrations (de Gouw et al., 2020). See Section S1 of the  
168 supplementary document for additional information and sensitivity tests regarding background VCD quantification.

## 169 **2.5 NO<sub>x</sub> Emission Inventories**

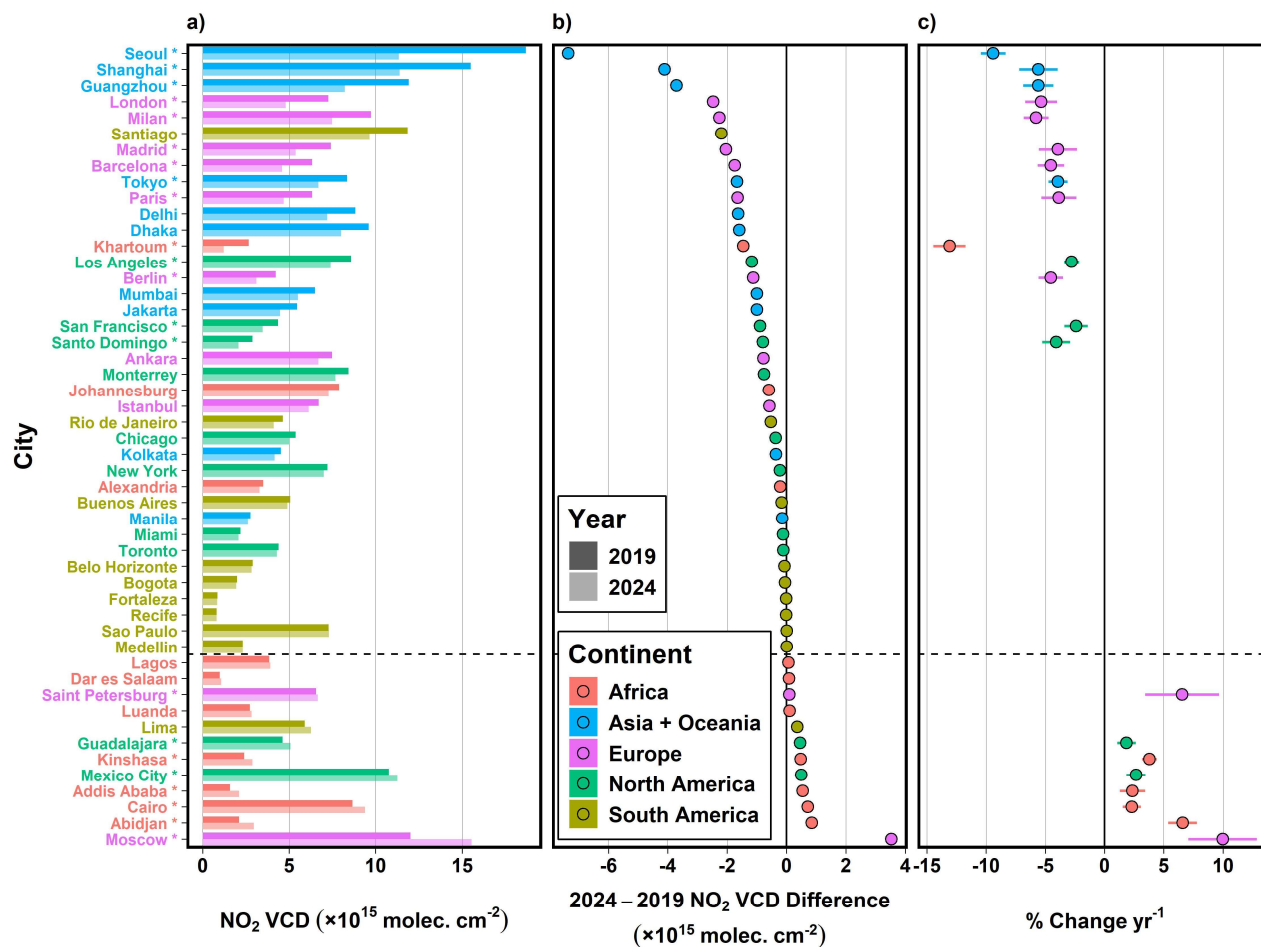
170 We use data from two inventories to evaluate NO<sub>x</sub> emissions: (1) version 8.1 of the Emissions Database for Global  
171 Atmospheric Research (EDGARv8.1; Crippa et al., 2024), and (2) the 2025 version of Community Emissions Data System  
172 (CEDS; Hoesly et al., 2025). EDGAR provides annual summed total and sector-specific NO<sub>x</sub> emissions at  $0.1^\circ \times 0.1^\circ$  spatial  
173 resolution globally, derived using a bottom-up method that combines sector-level activity data with corresponding emissions  
174 factors for energy generation, industrial sources, transportation, residential sources and agriculture, with data available through  
175 2022. CEDS is a similar bottom-up inventory, also provided at  $0.1^\circ \times 0.1^\circ$  spatial resolution, but provides emissions estimates  
176 at the monthly level through the end of 2023. Uncertainties are inherent in such emissions inventories, with a roughly 10-50%  
177 uncertainty when aggregating emissions to the country level, and even larger uncertainty for individual grid points (Crippa et  
178 al., 2018).

179 Like the handling of TROPOMI data (Sec. 2.3), we use GHS-SMOD to quantify annual NO<sub>x</sub> emissions for each urban cluster.

## 180 **3 Global VCD Changes from 2019 to 2024 in Major Urban Areas**

181 Using the method outlined in Section 2.2.1, the GHS-SMOD urban cluster boundaries are used to determine mean TROPOMI  
182 NO<sub>2</sub> concentrations for all urban clusters globally. Of all 11,534 GHS-SMOD urban clusters, 58.1% are in Asia and Oceania,  
183 18.5% are in Africa, 10.9% are in Europe, 6.2% are in North America and 6.3% are in South America. Looking at VCD  
184 changes from 2019 to 2024 in the 50 cities representing the ten most populous urban clusters on each continent, with Asia and  
185 Oceania considered jointly, East Asian cities represent four and European cities represent five of the ten largest VCD decreases  
186 (Fig. 2a). Seoul experienced the greatest absolute reduction in annual mean NO<sub>2</sub> VCD of any of these 50 cities (Fig. 2b),  
187 representing a significant decrease of  $-9.4 \pm 1.0\% \text{ yr}^{-1}$  ( $p < 0.001$ ; Fig. 2c). London, England produced the greatest NO<sub>2</sub> VCD  
188 decrease of the ten most populous European cities ( $-5.4 \pm 1.3\% \text{ yr}^{-1}$ ;  $p < 0.001$ ), occurring alongside the introduction of the  
189 city's ultra-low emission zone introduced in 2019 and expanded in 2023, which has contributed to decreased local NO<sub>2</sub>  
190 concentrations (Hajmohammadi and Heydecker, 2022).

191 None of the ten largest South American cities experienced statistically significant changes in NO<sub>2</sub> VCD, with relative changes  
192 typically less than  $\pm 0.6 \times 10^{15} \text{ molecules cm}^{-2}$  (Fig. 2b). The most notable exception is Santiago, Chile, which experienced an  
193 annual mean VCD difference of nearly  $-2.2 \times 10^{15} \text{ molecules cm}^{-2}$  between 2019 and 2024. Of the largest North American cities,  
194 significant decreases occurred in Los Angeles ( $-2.8 \pm 0.6\% \text{ yr}^{-1}$ ;  $p = 0.004$ ), and the San Francisco Bay Area ( $-2.8 \pm 0.6\% \text{ yr}^{-1}$ ;  $p$   
195  $= 0.023$ ), while significant increases occurred in the Mexican cities of Guadalajara ( $+1.9 \pm 0.8\% \text{ yr}^{-1}$ ;  $p = 0.019$ ) and Mexico  
196 City ( $+2.7 \pm 0.8\% \text{ yr}^{-1}$ ;  $p = 0.010$ ).



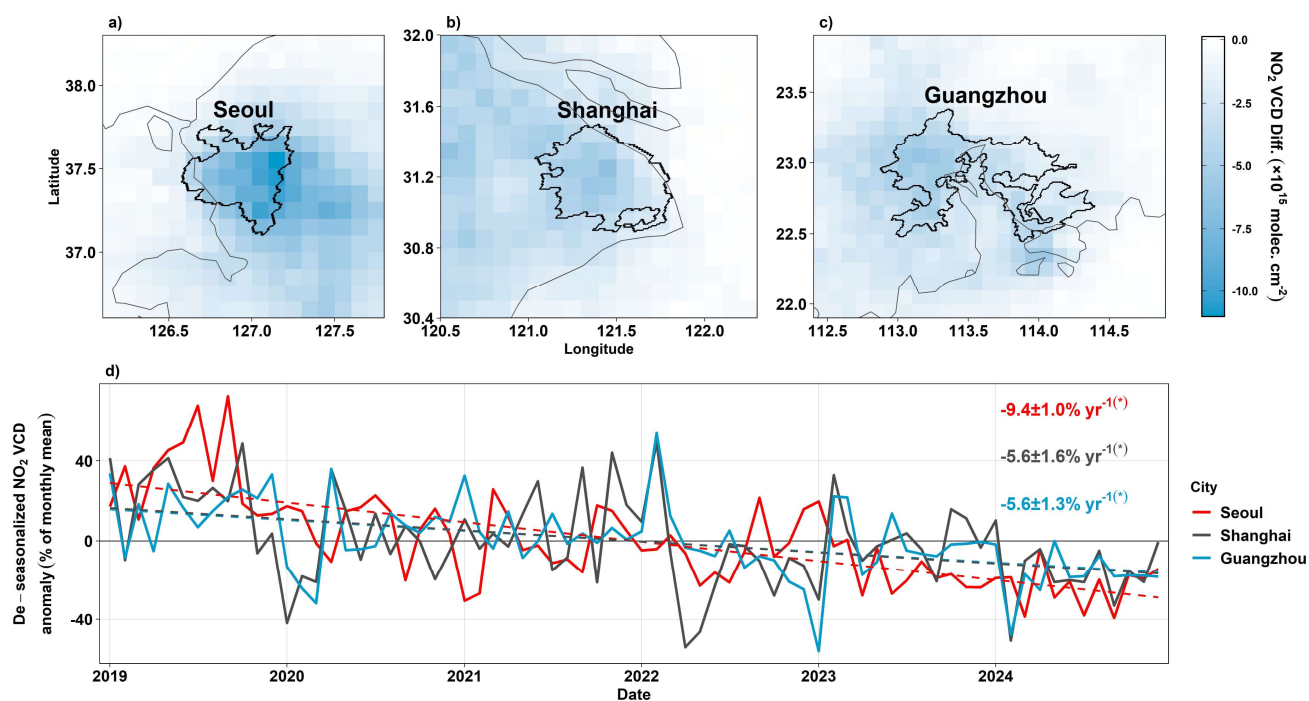
198

199 **Figure 2: (a) NO<sub>2</sub> VCD in 2019 (dark bars) and 2024 (light bars) for the 10 most populous urban clusters on each continent, based**  
 200 **on GHS-SMOD populations. (b) Absolute difference in NO<sub>2</sub> VCD for each city from 2019 to 2024. (c) NO<sub>2</sub> VCD percent change yr<sup>-1</sup>**  
 201 **from 2019 to 2024. Horizontal bars represent standard error, and colors correspond to the respective continent for each city. Cities**  
 202 **are ordered by magnitude of absolute VCD decrease. Statistical significance is denoted with an asterisk by each city name. Only**  
 203 **statistically significant results are reported in panel c.**

204 Most of the largest African cities experienced increased NO<sub>2</sub> VCDs from 2019 to 2024, with Abidjan, Ivory Coast experiencing  
 205 the largest urban increase ( $+6.6 \pm 1.2\%$  yr<sup>-1</sup>;  $p < 0.001$ ), with additional increases occurring in Cairo, Egypt ( $+2.3 \pm 0.8\%$  yr<sup>-1</sup>;  $p$   
 206  $= 0.006$ ); Addis Ababa, Ethiopia ( $+2.4 \pm 1.1\%$  yr<sup>-1</sup>;  $p = 0.012$ ); and Kinshasa, DR Congo ( $+3.8 \pm 0.6\%$  yr<sup>-1</sup>;  $p < 0.001$ ). In the  
 207 Sudanese capital of Khartoum, NO<sub>2</sub> VCDs started decreasing in 2023, coinciding with the onset of conflict within Sudan (Guo  
 208 et al., 2023; Fig. S10). This resulted in the largest absolute NO<sub>2</sub> VCD decrease of any African city from 2019 to 2024 (Fig.  
 209 2b), and a decrease of  $-13.1 \pm 1.4\%$  yr<sup>-1</sup> ( $p < 0.001$ ).

210 Of the cities presented in Fig. 2, the three largest absolute decreases between 2019 and 2024 were in the East Asian cities of  
 211 Seoul, South Korea (Fig. 3a); Shanghai, China (Fig. 3b); and Guangzhou, China (Fig. 3c). Decreases in Seoul coincide with  
 212 known policies implemented by the South Korean government since the early 2000s to reduce local emissions, as well as  
 213 changes in emissions that began following the COVID-19 pandemic (Ho et al., 2021; Seo et al. 2021). Moscow experienced  
 214 the largest NO<sub>2</sub> VCD increase of any large GHS-SMOD city through 2024, with a VCD increase of +9.97% yr<sup>-1</sup> (p=0.001).  
 215 This increase was accompanied by anomalously high monthly mean concentrations in early 2022 (Fig. S11), following the  
 216 onset of the Russia-Ukraine war in Ukraine, when monthly mean NO<sub>2</sub> VCDs for March reached  $59 \times 10^{15}$  molecules cm<sup>-2</sup> (see  
 217 Sec. 3.3).

218



219

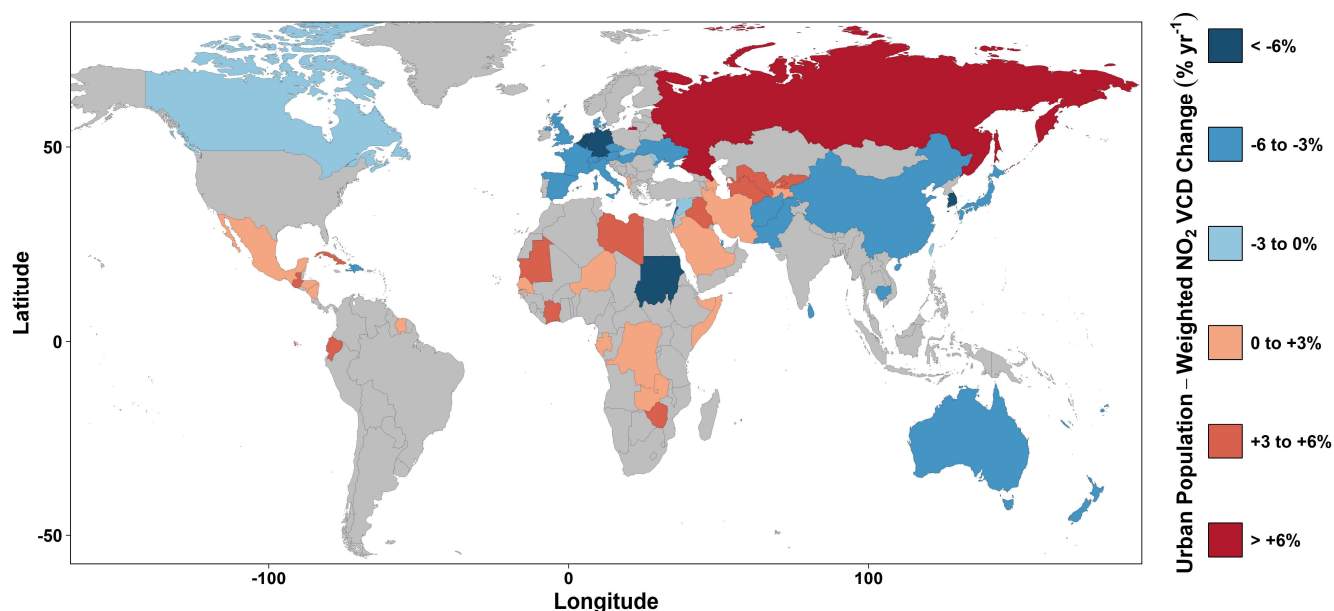
220 **Figure 3: Absolute change in mean annual NO<sub>2</sub> VCD from 2019 to 2024 for three East Asian cities: (a) Seoul, South Korea, (b)**  
 221 **Shanghai, China and (c) Guangzhou, China. Colors in panels a-c show magnitude of VCD change, thin lines show national borders**  
 222 **or coastlines, and thick lines show the GHS-SMOD urban boundary. (d) Solid lines show de-seasonalized monthly VCD anomaly**  
 223 **from 01/2019 through 12/2024, colored by city. Dashed lines are produced from ordinary least-squares regression. The % change**  
 224 **yr<sup>-1</sup>, standard error and statistical significance is reported in the top right of panel d.**

#### 225 4 Population-weighted Country-level Urban TROPOMI NO<sub>2</sub>

226 Aggregating the NO<sub>2</sub> VCD changes to the country level by considering the population of each urban cluster (Eq. 1), we identify  
 227 population-weighted VCD changes in countries globally (Fig. 4). The majority of urban NO<sub>2</sub> VCD increases were observed in  
 228 much of Central America including Mexico, in Africa, in the Middle East and in Central Asia. Russia experienced the largest

229 population-weighted VCD increase of  $6.2 \pm 3.6\% \text{ yr}^{-1}$  ( $p = 0.046$ ). Broad urban VCD decreases were observed in numerous  
230 countries across Western and Central Europe, as well as Eastern Asian countries. The largest urban population-weighted  
231 decrease occurred in South Korea ( $-8.74 \pm 0.9\% \text{ yr}^{-1}$ ;  $p < 0.001$ ).

232



233

234 **Figure 4: Global spatial representation of the urban population-weighted NO<sub>2</sub> VCD % change yr<sup>-1</sup> from 2019 to 2024. Gray fill**  
235 **denotes statistical insignificance ( $p > 0.05$ ).**

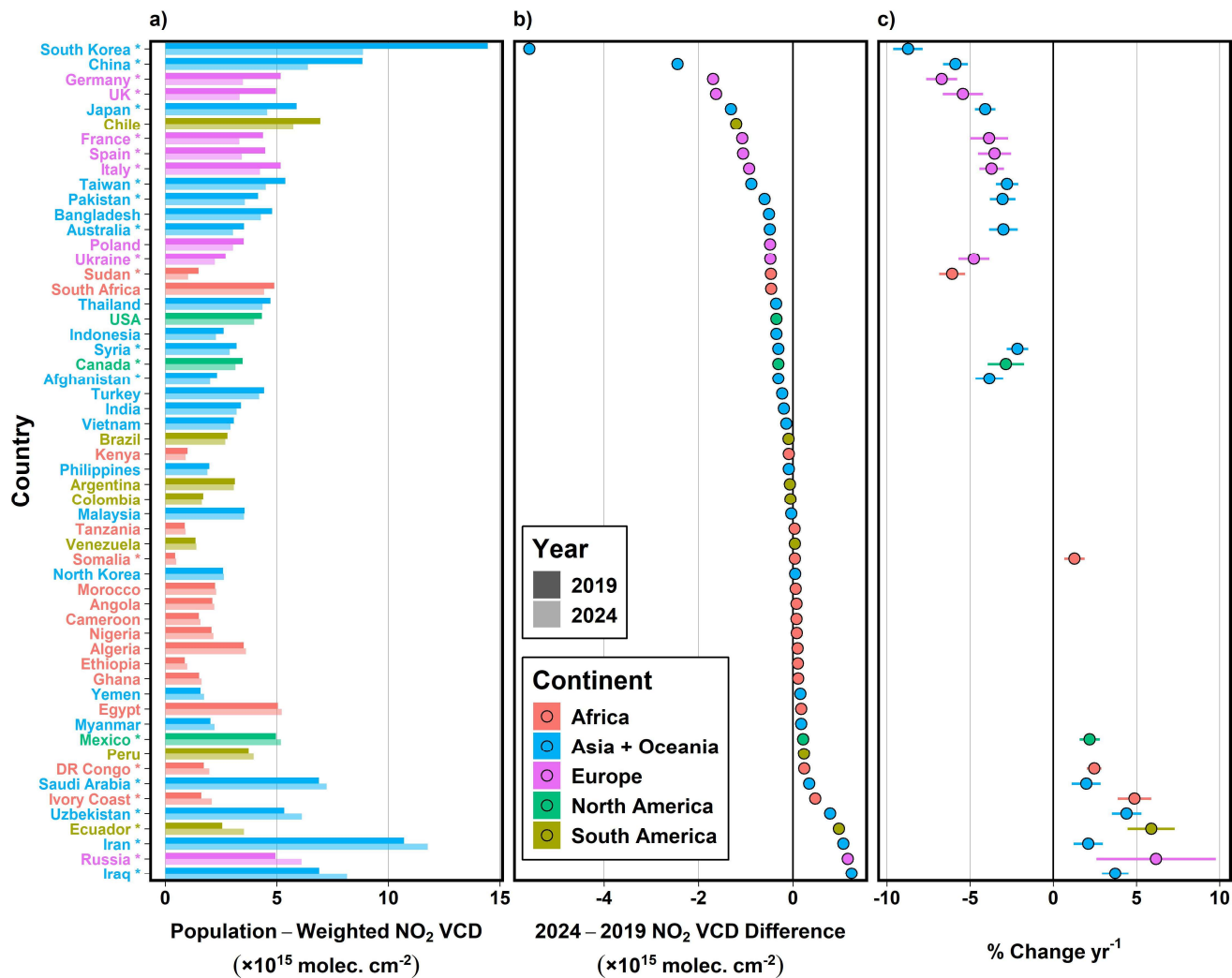
236 Much of the Middle East exhibited substantial increases in urban population-weighted NO<sub>2</sub> VCDs from 2019 to 2024, including  
237 in Saudi Arabia ( $+2.0 \pm 0.9\% \text{ yr}^{-1}$ ;  $p = 0.009$ ), Iraq ( $+3.7 \pm 0.8\% \text{ yr}^{-1}$ ;  $p < 0.001$ ), and Iran ( $+2.1 \pm 0.9\% \text{ yr}^{-1}$ ;  $p = 0.013$ ), with broad  
238 increases that extend beyond the urban environment. One of the most salient VCD decreases in the Middle East occurred in  
239 Lebanon ( $-8.5 \pm 1.0\% \text{ yr}^{-1}$ ;  $p < 0.001$ ), coinciding with the country's severe economic and financial crisis that began in late 2019  
240 (Harake et al., 2019). VCD decreases through 2024 were particularly stark in the Lebanese capital Beirut ( $-7.9 \pm 1.1\% \text{ yr}^{-1}$ ;  
241  $p < 0.001$ ). Additional Middle Eastern countries that exhibited decreased urban NO<sub>2</sub> VCDs through 2024 include much of Israel  
242 ( $-4.5 \pm 0.9\% \text{ yr}^{-1}$ ;  $p < 0.001$ ), Qatar ( $-3.4 \pm 1.2\% \text{ yr}^{-1}$ ;  $p = 0.004$ ), and Afghanistan ( $-3.8 \pm 0.8\% \text{ yr}^{-1}$ ;  $p = 0.003$ ). Notable urban NO<sub>2</sub>  
243 VCD changes in less populated countries of Asia and Oceania include decreases in Cambodia ( $-5.0 \pm 0.9\% \text{ yr}^{-1}$ ;  $p < 0.001$ ), Sri  
244 Lanka ( $-5.4 \pm 0.9\% \text{ yr}^{-1}$ ;  $p < 0.001$ ) and Australia ( $-3.0 \pm 0.9\% \text{ yr}^{-1}$ ;  $p = 0.008$ ). Urban increases were observed in much of Central  
245 Asia, including Uzbekistan ( $+4.4 \pm 0.9\% \text{ yr}^{-1}$ ;  $p < 0.001$ ) and Turkmenistan ( $+4.5 \pm 0.5\% \text{ yr}^{-1}$ ;  $p < 0.001$ ).

246 NO<sub>2</sub> VCD decreases for more populous countries with an urban population of at least nine million were largest in East Asia,  
247 including China ( $-6.0 \pm 1.0\% \text{ yr}^{-1}$ ;  $p < 0.001$ ) and Japan ( $-4.1 \pm 0.6\% \text{ yr}^{-1}$ ;  $p < 0.001$ ) (Fig. 5). Urban population-weighted VCD  
248 decreases in South Korea were particularly pronounced, with a population-weighted concentration difference of  $-5.6 \times 10^{15}$   
249 molecules cm<sup>-2</sup> between 2019 and 2024. In South Asia, the neighboring countries of Afghanistan ( $-3.8 \pm 0.8\% \text{ yr}^{-1}$ ;  $p = 0.003$ )

250 and Pakistan ( $-3.0 \pm 0.8\% \text{ yr}^{-1}$ ;  $p=0.012$ ) exhibited some of the only significant country-level VCD decreases for the region.  
251 Significant decreases also occurred in numerous countries of Western and Central Europe, with Germany experiencing the  
252 largest VCD decrease in Europe through 2024 ( $-6.7 \pm 0.9\% \text{ yr}^{-1}$ ;  $p < 0.001$ ). Of the most-populous European countries, Russia  
253 was the only country to experience increased population-weighted  $\text{NO}_2$  VCDs through 2024.

254 A majority of larger African countries exhibited insignificant urban VCD changes, with 2024 population-weighted VCDs  
255 changing by less than  $0.25 \times 10^{15}$  molecules  $\text{cm}^{-2}$  relative to 2019 levels (Fig. 5b). Exceptions include larger changes in Sudan  
256 ( $-6.1 \pm 0.8\% \text{ yr}^{-1}$ ;  $p < 0.001$ ) and Ivory Coast ( $+4.9 \pm 1.0\% \text{ yr}^{-1}$ ;  $p < 0.001$ ). Middle Eastern and Central Asian countries  
257 experienced some of the largest urban VCD increases, with Iraq experiencing the largest difference between 2019 and 2024  
258 levels of any larger country ( $+1.2 \times 10^{15}$  molecules  $\text{cm}^{-2}$ ). Chile saw the largest difference in annual mean urban  $\text{NO}_2$  VCD  
259 between 2019 and 2024 of any South American country, due in large part to lower 2024 annual mean  $\text{NO}_2$  VCDs in the capital  
260 city of Santiago (Fig. 5b).

261



262

263 Figure 5: Same as Fig. 2 but presenting changes in country-level urban population-weighted NO<sub>2</sub> VCDs for countries with an urban  
 264 population of at least nine million, based on urban cluster populations provided from GHS-SMOD.

265 **5 Regional TROPOMI NO<sub>2</sub> Vertical Column Densities from 2019 to 2024**

266 The following subsections describe NO<sub>2</sub> VCDs in five global subregions: Asia and Oceania, Africa, Europe, North America  
 267 and South America

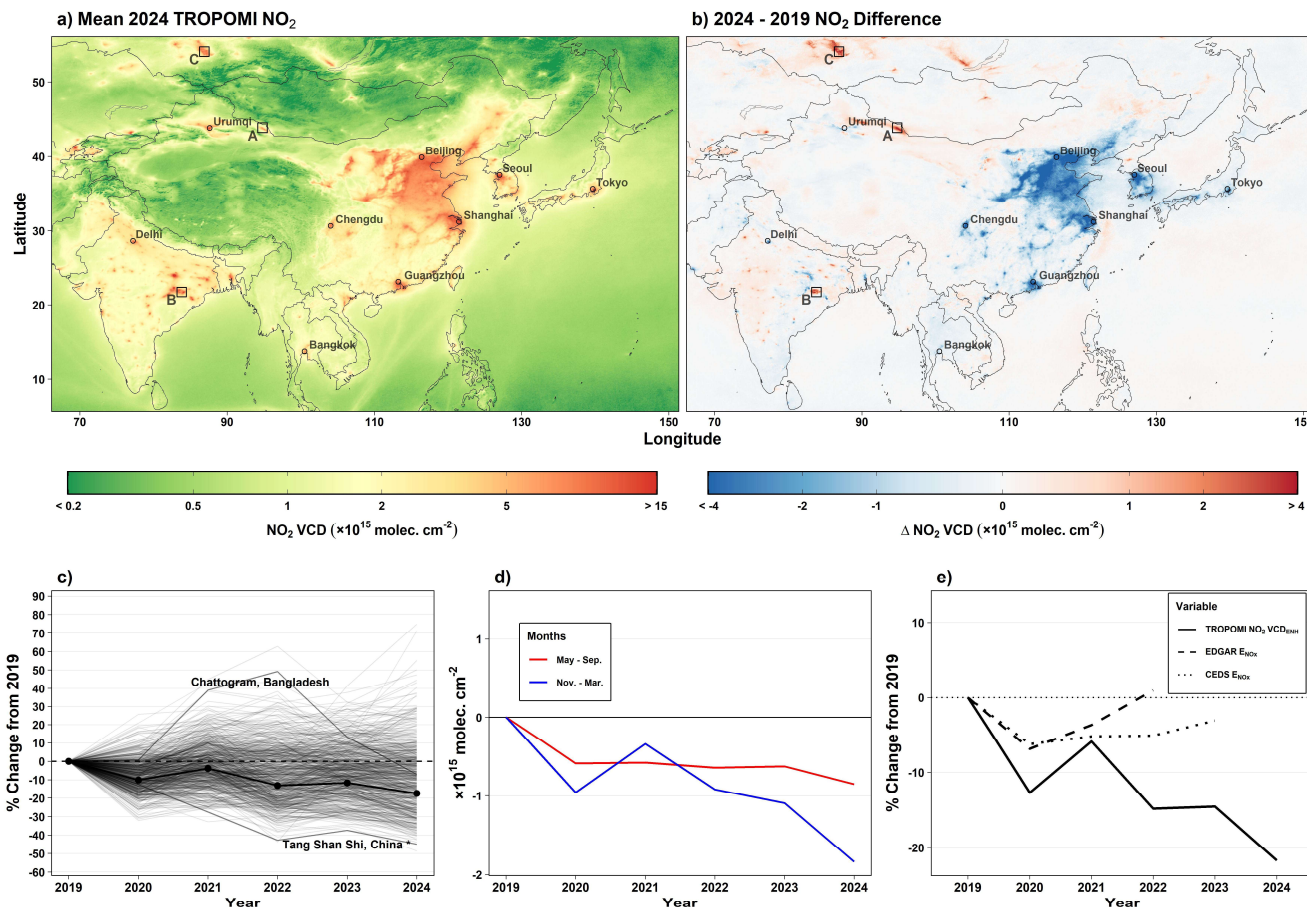
268 **5.1 Asia and Oceania**

269 North and East China, one of the most populated regions globally with approximately 11% of the 1000 largest GHS-SMOD  
 270 cities, produced the broadest continuous expanse of 2024 annual mean NO<sub>2</sub> VCDs at or above  $5 \times 10^{15}$  molecules cm<sup>-2</sup> (Fig.

271 6a). Despite this, substantial VCD decreases were observed in this region from 2019 to 2024 (Fig. 6b). NO<sub>2</sub> concentrations  
272 had already been decreasing in China prior to 2019 (Liu et al., 2016; de Foy et al., 2016), and the decrease continued after the  
273 onset of the COVID-19 pandemic, during which numerous lockdowns throughout the country between 2020 and 2022 led to  
274 reduced NO<sub>2</sub> concentrations (Zheng et al., 2021; Cooper et al., 2022; Levelt et al., 2022; Ma et al., 2023; Zhao et al., 2024).  
275 The decrease in NO<sub>2</sub> also coincided with general Chinese government policies directed at reducing emissions, including stricter  
276 emissions controls for industrial sources, energy generation and the transportation sector (Shi et al., 2022; Li et al., 2024).

277 In India, the largest differences in urban NO<sub>2</sub> VCD between 2019 and 2024 were observed in Delhi ( $-1.6 \times 10^{15}$  molecules cm<sup>-</sup>  
278 <sup>2</sup>) and Mumbai ( $-1.0 \times 10^{15}$  molecules cm<sup>-2</sup>), though neither city exhibited statistically significant decreases over that period.  
279 Elevated NO<sub>2</sub> near numerous coal-fired power plants and coal mines is a common feature in India (Panda et al., 2023),  
280 evidenced by the many apparent point sources in the 2024 annual average TROPOMI VCDs throughout the country (Fig. 6a).  
281 NO<sub>2</sub> VCDs increased at many of these points sources from 2019 to 2024 (Fig. 6b), suggesting an increase in emissions from  
282 energy production and use. In the Middle East and Central Asia, urban regions experienced some of the highest NO<sub>2</sub> VCDs  
283 globally in the TROPOMI record (Fig. 7). The Iranian capital of Tehran by far has the largest annual average VCD in the  
284 TROPOMI tropospheric NO<sub>2</sub> record for all GHS-SMOD cities, with annual mean values remaining above  $30 \times 10^{15}$  molecules  
285 cm<sup>-2</sup> throughout the entirety of the TROPOMI record (Fig. S12).

286

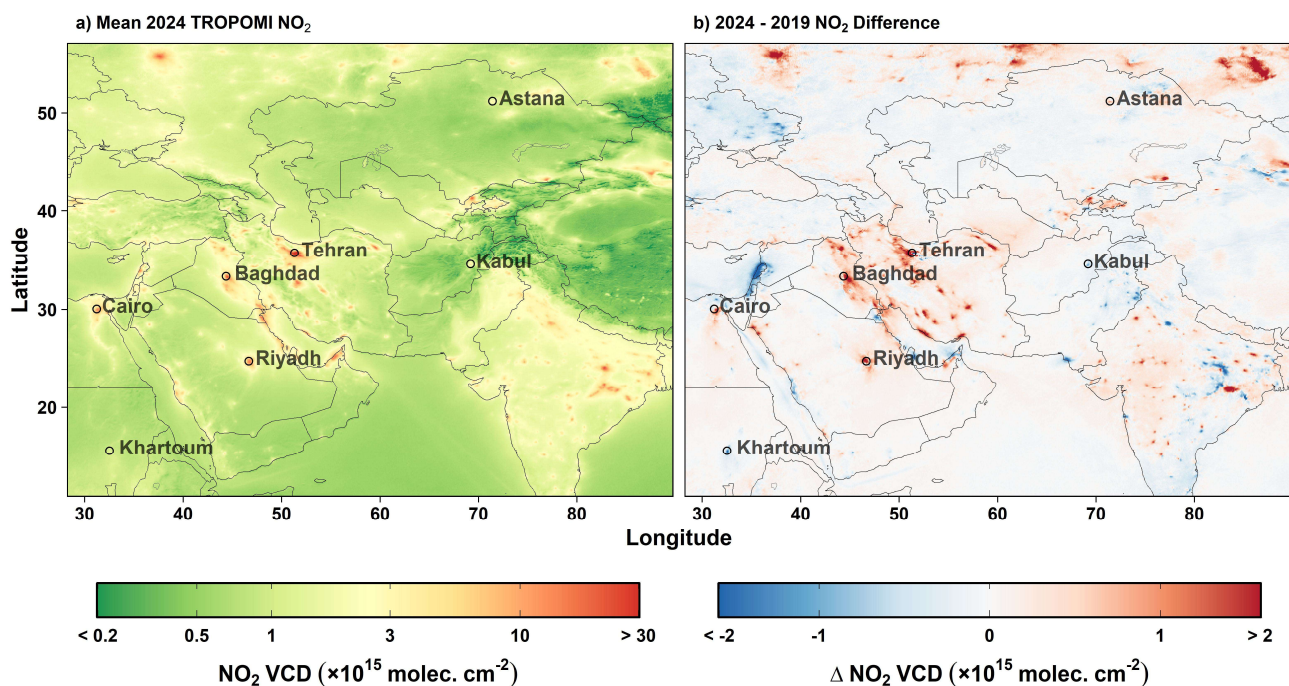


287

288 **Figure 6: (a) Mean 2024 TROPOMI NO<sub>2</sub> VCDs and (b) relative difference in annual mean TROPOMI VCDs between 2019 and**  
 289 **2024, centered on South and East Asia. Regions A, B and C represent the Santanghu Basin, the Ib Valley and Kuzbass mining**  
 290 **regions, respectively, as highlighted in Fig. 12. (c) Population-weighted percent difference in annual mean TROPOMI NO<sub>2</sub> VCD**  
 291 **relative to 2019 levels for all GHS-SMOD urban clusters in Asia and Oceania (solid black line), and percent change in VCD for**  
 292 **individual clusters with a population of at least 500,000 (gray lines). Asterisks denote statistical significance. (d) Absolute population-**  
 293 **weighted difference in VCD for urban clusters in Asia and Oceania in May-September (red line) and November to March (blue line).**  
 294 **(e) Relative difference in population-weighted TROPOMI NO<sub>2</sub> urban enhancement (VCD<sub>ENH</sub>; solid line, 2019-2024), NO<sub>x</sub> emissions**  
 295 **from the EDGARv8.1 emissions inventory (dashed line, 2019-2022) and CEDS emissions inventory (dotted line, 2019-2023).**

296 Across Asia and Oceania as a whole, which contain a majority of all urban clusters globally, population-weighted NO<sub>2</sub> VCDs  
 297 were approximately 17% lower in 2024 than in 2019 (Fig. 6c). One notable decrease in Asia occurred in the Chinese city of  
 298 Tang Shan Shi, located to the east of Beijing, which experienced an NO<sub>2</sub> VCD decrease of nearly 45% from 2019 to 2024. The  
 299 largest increase in Asia through 2024 occurred in the Mongolian capital of Ulaanbaatar, where the 2024 mean VCD was more  
 300 than 70% larger than in 2019. Numerous Bangladeshi cities, including Chattogram, experienced substantially increased VCDs  
 301 from 2020 through 2022, with VCDs decreasing again by 2024 to the near 2019 levels (Fig. S13).

302 Different seasons can have outside impact on the relative change in annual NO<sub>2</sub> VCD. In cities of Asia and Oceania, the bulk  
 303 of the observed annual decreases through 2024 occurred during November – March (Fig. 6d), with a population-weighted  
 304 decrease of  $-1.8 \times 10^{15}$  molecules cm<sup>-2</sup>. Although the absolute changes in November – March were larger than in May –  
 305 September, the relative percent changes for the two periods were more comparable (Fig. S14).  
 306



307  
 308 **Figure 7: (a) Mean 2024 TROPOMI NO<sub>2</sub> VCDs and (b) relative difference in annual mean TROPOMI VCDs between 2019 and**  
 309 **2024, centered on the Middle East and Central Asia.**

310 Urban NO<sub>2</sub> concentrations are not only influenced by local emissions, but also by advection of upwind pollutants into the urban  
 311 boundary. We account for the role that upwind background concentrations may play in urban NO<sub>2</sub> concentrations by identifying  
 312 changes in the urban enhancement of NO<sub>2</sub> (VCD<sub>ENH</sub>), represented by the difference between NO<sub>2</sub> VCDs in the urban cluster  
 313 and the urban background VCD. By removing the background concentrations, we expect that the percent change in VCD<sub>ENH</sub>  
 314 relative to a baseline year can be primarily attributed to changes in local, urban NO<sub>x</sub> emissions. We then evaluate changes in  
 315 VCD<sub>ENH</sub> against changes in gridded NO<sub>x</sub> emissions inventories from (1) the EDGARv8.1, with data available through 2022  
 316 and (2) CEDS, with data available through 2023 (Fig. S15).

317 In Asia and Oceania, cities experienced sustained decreases in VCD<sub>ENH</sub>, with population-weighted values 22.7% lower in 2024  
 318 than in 2019 (Fig. 6e). Cities in Asia and Oceania experienced VCD<sub>ENH</sub> that tracked relatively well with both inventories from  
 319 2019 to 2021, with a mean difference of +4.0% (EDGARv8.1) and +3.6% (CEDS) between emissions and VCD<sub>ENH</sub>. However,  
 320 in 2022, EDGARv8.1 showed increased emissions and CEDS exhibited mostly unchanged emissions, while VCD<sub>ENH</sub> exhibited

321 a sharp decrease for that year. This resulted in a percentage difference of +15.8% (EDGARv8.1) and +9.7% (CEDDS) between  
322 emissions and  $VCD_{ENH}$  in 2022 relative to 2019 levels (Fig. 6e). The 2022  $VCD_{ENH}$  decrease coincided with broad lockdowns  
323 in China related to the COVID-19 pandemic, suggesting that EDGAR emissions may not reflect emissions decreases during  
324 that lockdown period.

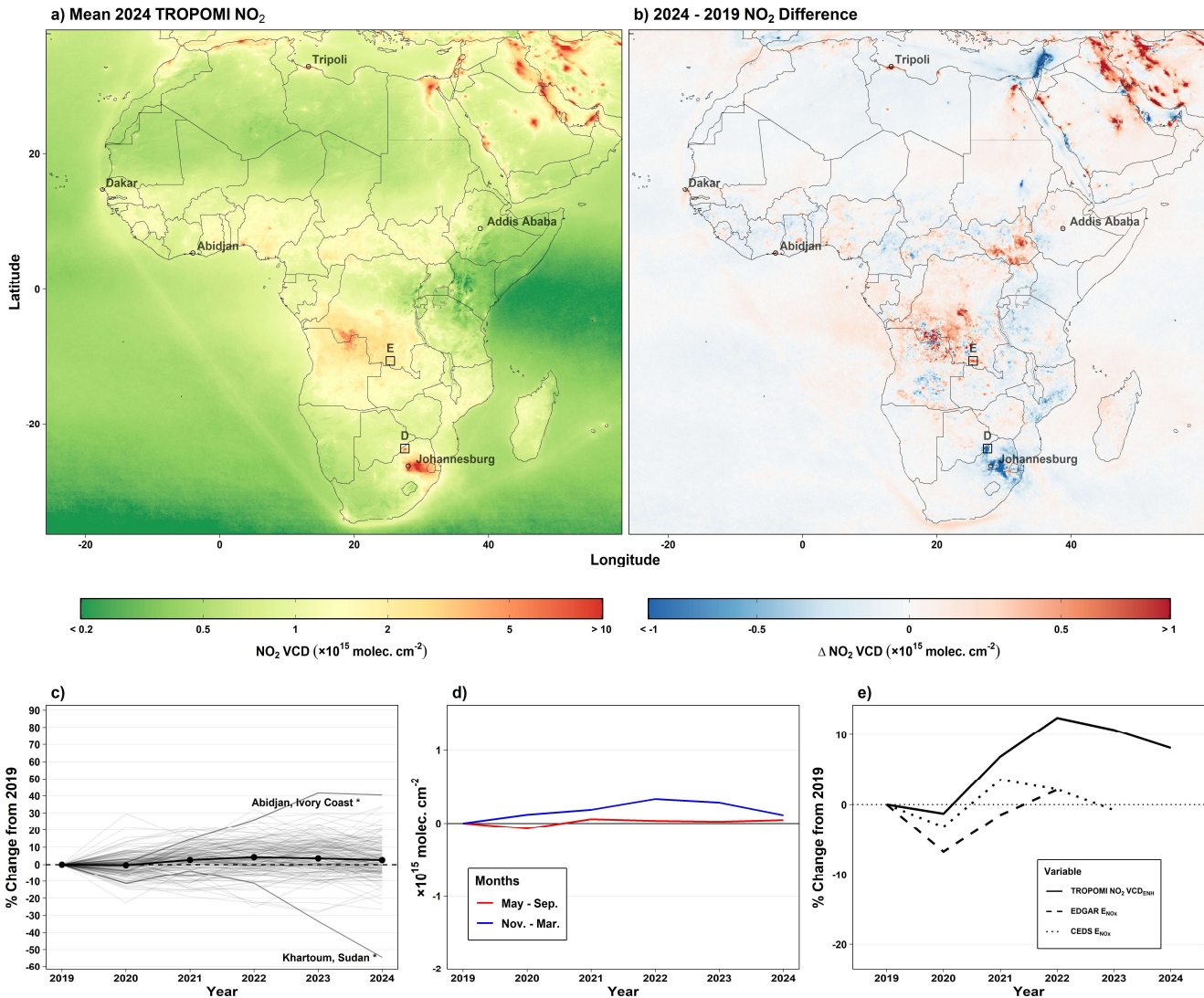
## 325 5.2 Africa

326 Areas to the east of Johannesburg, South Africa and the surrounding region exhibited the broadest enhanced  $NO_2$  VCD for the  
327 African continent in 2024 (Fig. 8a). Numerous surface coal mines and coal-fired power plants, particularly to the east of  
328 Johannesburg, contribute to the region's  $NO_2$  signature (Shikwambana et al., 2020). Cairo, Egypt represents the largest urban  
329  $NO_2$  signature of any major urban region in Africa in 2024, when the annual mean  $NO_2$  VCD reached  $9.4 \times 10^{15}$  molecules  
330  $cm^{-2}$ . From 2019 to 2024, Cairo experienced a statistically significant VCD increase of  $2.3 \pm 0.8\% \text{ yr}^{-1}$  ( $p = 0.006$ ). Along the  
331 African Mediterranean coast, most urban areas showed increased  $NO_2$  VCDs through 2024.

332 Through 2024, African cities experienced a gradual increase in population-weighted  $NO_2$  VCD (Fig. 8c). The largest percent  
333 increase occurred in Abidjan, the capital city of Ivory Coast, which experienced an increase in  $NO_2$  VCD of more than 40%  
334 from 2019 through 2024. Khartoum, Sudan experienced the largest percent decrease of any large African City, with mean 2024  
335 levels nearly 60% lower than in 2019.

336 In African cities (Fig. 8d), population-weighted VCDs during November-March were  $0.1 \times 10^{15}$  molecules  $cm^{-2}$  larger in 2024  
337 than 2019, with little to no change occurring on average during May – September. When evaluating changes in  $VCD_{ENH}$  in  
338 African cities, population-weighted  $VCD_{ENH}$  were +8.1% larger in 2024 relative to 2019 levels (Fig. 8e). One distinct feature  
339 for African cities is the lack of a pronounced decrease in  $VCD_{ENH}$  during 2020, coinciding with the onset of the COVID-19  
340 pandemic, a feature observed on all other continents. Evaluating  $NO_x$  emissions inventories in African cities, we find a mean  
341 difference of -8.0% (EDARv8.1) and -6.7% (CEDDS) between inventory  $NO_x$  emission and  $VCD_{ENH}$  changes, indicating a  
342 potential underestimate in both emissions inventories in African cities for this period.

343

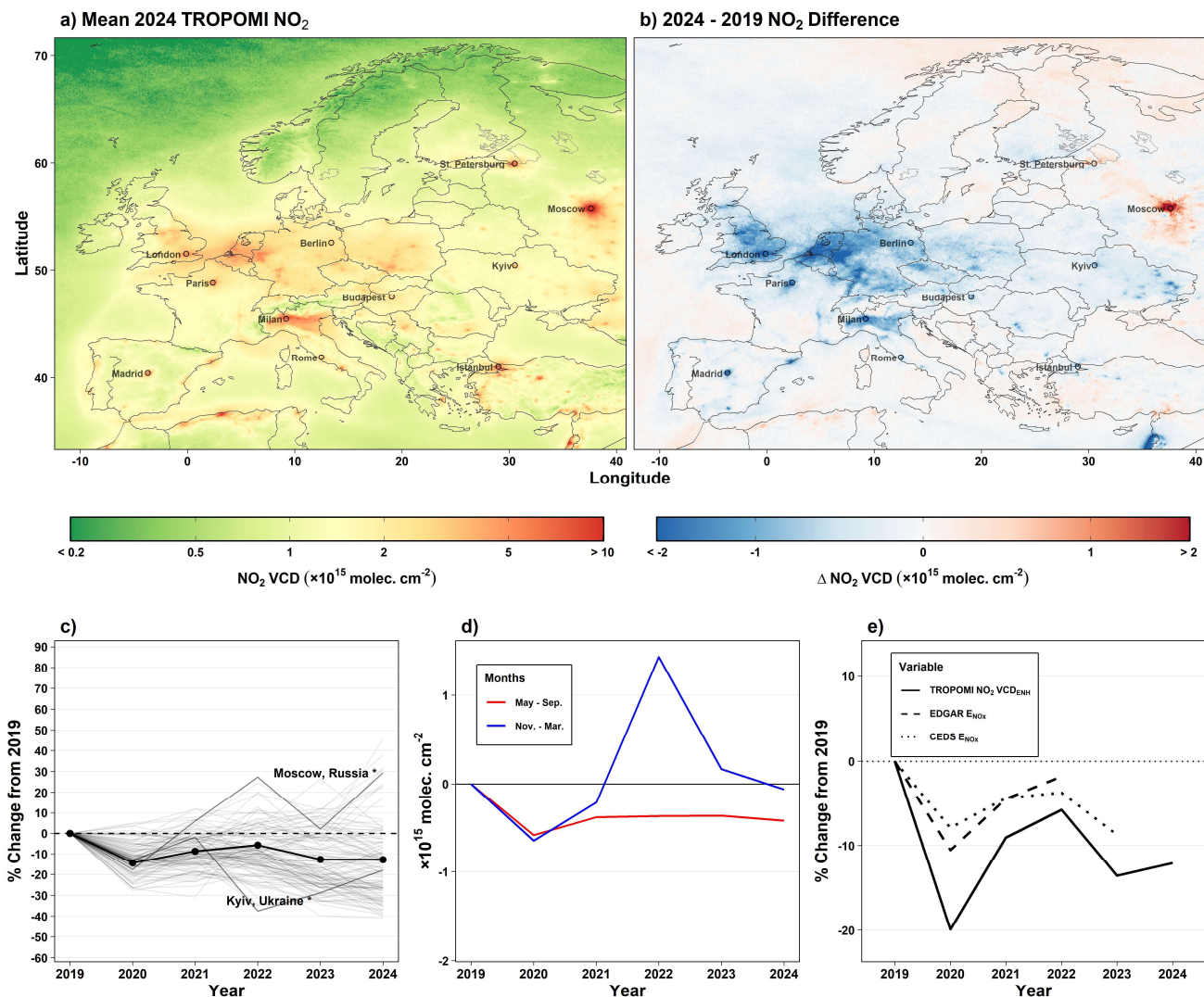


344

345 **Figure 8:** Same as Fig. 6, but for the African continent. Regions D and E in panels a and b represent the Grootegeluk and Kolwezi  
 346 mines, respectively, as highlighted in Fig. 12.

347 **5.3 Europe**

348 NO<sub>2</sub> VCDs in Europe were largest in urban areas, with the largest 2024 mean VCD occurring in Moscow, Russia ( $15.5 \times 10^{15}$   
 349 molecules cm<sup>-2</sup>) (Fig. 9a). Broad enhanced 2024 annual mean VCDs exceeding  $4 \times 10^{15}$  molecules cm<sup>-2</sup> were observed in a  
 350 region encompassing Belgium, the Netherlands and western portions of Germany, with values exceeding  $5 \times 10^{15}$  molecules  
 351 cm<sup>-2</sup> in the Po River Valley of northern Italy.



352  
353 **Figure 9: Same as Fig. 6, but for Europe.**

354 Of the 1257 urban clusters in Europe, 1007 (80%) exhibited lower VCDs in 2024 than in 2019. Of the 53 European urban  
 355 clusters with a population greater than 1,000,000, 2024 VCDs were lower than 2019 VCDs in 48 (91%), with the exception of  
 356 Moscow and other cities of western Russia, which experienced increases (Fig. 9b). The broad decreases across large European  
 357 cities are likely due to a combination of (1) a decrease in emissions that continued following the COVID-19 pandemic, (2)  
 358 continued transition to alternative energy sources following the start of the Russia-Ukraine war in 2022 and (3) existing policies  
 359 implemented within the EU (Matthias et al., 2021; Rokicki et al., 2023; Cifuentes-Faura, 2022). These policies include the

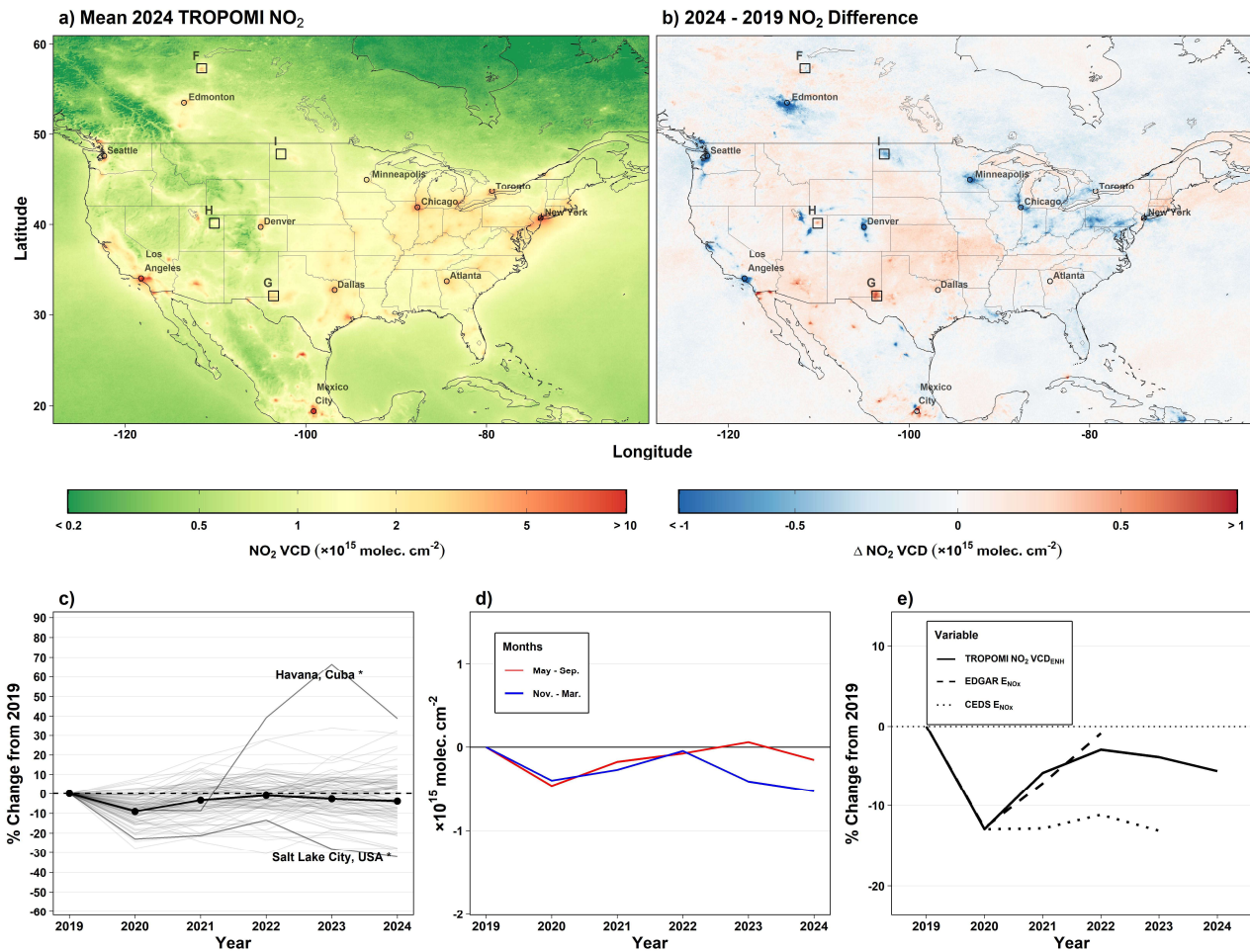
360 European Green Deal and European Climate Law, which promote zero-emission vehicles, stricter vehicle emissions targets  
361 and updated industrial emissions regulations.

362 European cities experienced the most pronounced decrease in column  $\text{NO}_2$  of any continent in 2020, with population-weighted  
363 VCDs decreases by 16% from 2019 to 2020 (Fig. 9c). Previous work has attributed such decreases to the COVID-19 pandemic  
364 (Cooper et al., 2022; Levelt et al., 2022).  $\text{NO}_2$  VCDs rebounded marginally in 2021 and 2022, followed by decreases into 2023  
365 and 2024. Decreases are more pronounced when only analyzing cities in the 27 member countries of the European Union (Fig.  
366 S16). One notable feature within the European annual average VCDs is the contrasting VCD directionality in Russian and  
367 Ukrainian cities in 2022, at the onset of the Russia-Ukraine War (Fig. S17). In the Ukrainian capital of Kyiv, annual VCDs  
368 dropped nearly 40% in 2022 relative to 2019, coinciding with a large portion of the city fleeing due to conflict in and near the  
369 city. To contrast this, VCDs increased nearly 30% in the Russian capital of Moscow during the same period. Following 2022,  
370 VCDs in Kyiv increased steadily, while in Moscow, levels decreased in 2023 then increased again in 2024.

371 Population-weighted May – September VCDs decreased by  $0.4 \times 10^{15}$  molecules  $\text{cm}^{-2}$  (-10%) through 2024, while VCD  
372 behavior during November – March has been less consistent, despite a sharp increase in winter-time levels in 2022 during the  
373 onset of the Russia-Ukraine war (Fig. 9d). We note that the seasonal changes in Europe show more comparable winter and  
374 summer changes if evaluating with Russian cities removed (Fig. S18). When accounting for background concentrations,  
375  $\text{VCD}_{\text{ENH}}$  in European cities experienced the largest drop in 2020 of any continent, with population-weighted  $\text{VCD}_{\text{ENH}}$   
376 decreasing by -20% from 2019 to 2020 (Fig. 9e). While both EDGARv8.1 and CEDS exhibited similar mean year to year  
377 variability as  $\text{VCD}_{\text{ENH}}$  in European cities, changes in the inventories appeared underestimated, with each inventory estimate  
378 exhibiting a mean percent difference relative to  $\text{VCD}_{\text{ENH}}$  of +6.0 and +5.9%, respectively. This suggests a slight underestimate  
379 in emissions inventory decreases in European cities relative to observed  $\text{VCD}_{\text{ENH}}$  levels.

#### 380 **5.4 North America**

381 Throughout North America, 2024 annual mean  $\text{NO}_2$  VCDs were largest in urban regions, including Los Angeles ( $7.4 \times 10^{15}$   
382 molecules  $\text{cm}^{-2}$ ), New York ( $7.0 \times 10^{15}$  molecules  $\text{cm}^{-2}$ ), and Mexico City ( $11.3 \times 10^{15}$  molecules  $\text{cm}^{-2}$ ), as well as near fossil  
383 fuel-fired power plant and mining operations (Fig. 10a). Most major cities in the U.S. and Canada exhibited decreased or  
384 unchanged  $\text{NO}_2$  VCDs (Fig. 10b). Phoenix, Arizona was one notable exception to these decreases, with mean 2024 VCDs 10%  
385 higher than in 2019 (Fig. S19).



386

387 **Figure 10: Same as Fig. 6, but for North America. Regions F, G, H and I in panels a and b represent the Athabasca, Permian, Bakken**  
 388 **and Uintah, respectively, as highlighted in Fig. 12.**

389 In Canada, the largest difference in VCD between 2024 and 2019 occurred in Alberta Province in and around Edmonton ( $-0.9$   
 390  $\times 10^{15}$  molecules  $\text{cm}^{-2}$ ; Fig. 10b), although decreases were not statistically significant for that period. In the U.S., aside from  
 391 decreases in urban environments, the largest changes were observed in remote areas near coal power plants with reduced  
 392 activity, e.g. near the decommissioned Navajo Generating Station in northern Arizona (Goldberg et al., 2021). Apparent within  
 393 the U.S. is a slight increase in background concentrations in rural regions, particularly in the Central and Western U.S. It is  
 394 unclear if this is due to an extension of the  $\text{NO}_2$  lifetime due to decreasing VOCs and  $\text{O}_3$  over this 6-year period (e.g., Laughner  
 395 & Cohen 2019) or due to increased  $\text{NO}_x$  emissions in rural areas or both. Further work should investigate this.

396 In Mexico, Central America and the Caribbean, the largest VCDs are observed near Mexico City ( $11.3 \times 10^{15}$  molecules  $\text{cm}^{-2}$ )  
 397 and Monterrey, Mexico ( $7.7 \times 10^{15}$  molecules  $\text{cm}^{-2}$ ), with numerous other notable urban signatures (Fig. 10a). The largest

398 urban increases were observed at sites in Northern Mexico, including Mexicali ( $+6.1 \pm 0.9\%$  yr<sup>-1</sup>;  $p < 0.001$ ) and Hermosillo  
399 ( $+5.2 \pm 0.7\%$  yr<sup>-1</sup>;  $p < 0.001$ ). Additional notable changes occurred in the capital city of Santo Domingo, Dominican Republic  
400 ( $-4.1 \pm 1.2\%$  yr<sup>-1</sup>;  $p = 0.006$ ), and Havana, Cuba ( $+11.2 \pm 1.7\%$  yr<sup>-1</sup>;  $p < 0.001$ ) (Fig. 10b).

401 Most North American cities experienced a decrease in annual NO<sub>2</sub> VCD of less than 10% in 2020, with concentrations  
402 generally rebounding to 2019 levels by 2024 (Fig. 10c). Havana, Cuba was a notable exception of North American cities, with  
403 VCDs increasing by nearly 70% through 2023 relative to 2019, with a slight decrease in 2024. Cities in the western U.S., such  
404 as Salt Lake City and Denver experienced some of the largest percent decreases on the continent, decreasing by approximately  
405 30% through 2024. The bulk of the observed annual decreases through 2024 in North American cities occurred during winter  
406 (Fig. 10 d), with an average winter decrease of  $-0.5 \times 10^{15}$  molecules cm<sup>-2</sup> during those months. In North America, VCD<sub>ENH</sub>  
407 decreased by 13% from 2019 to 2020 (Fig. 10e), compared with a decrease of 10% in overall urban VCD from 2019 to 2020,  
408 and VCD<sub>ENH</sub> remained approximately 7.5% below 2019 levels by 2024. Averaged for North America, population-weighted  
409 EDGAR NO<sub>x</sub> emissions and VCD<sub>ENH</sub> exhibited a similar change relative to 2019 levels through 2022, with a mean difference  
410 of +0.3%, while CEDS and VCD<sub>ENH</sub> exhibited a larger mean difference of -6.1%, with differences most pronounced after 2020.  
411 This suggests relatively good agreement between North American EDGAR and TROPOMI relative changes, while CEDS  
412 emissions for the region may be underestimated from 2020 onward (Fig. 10e).

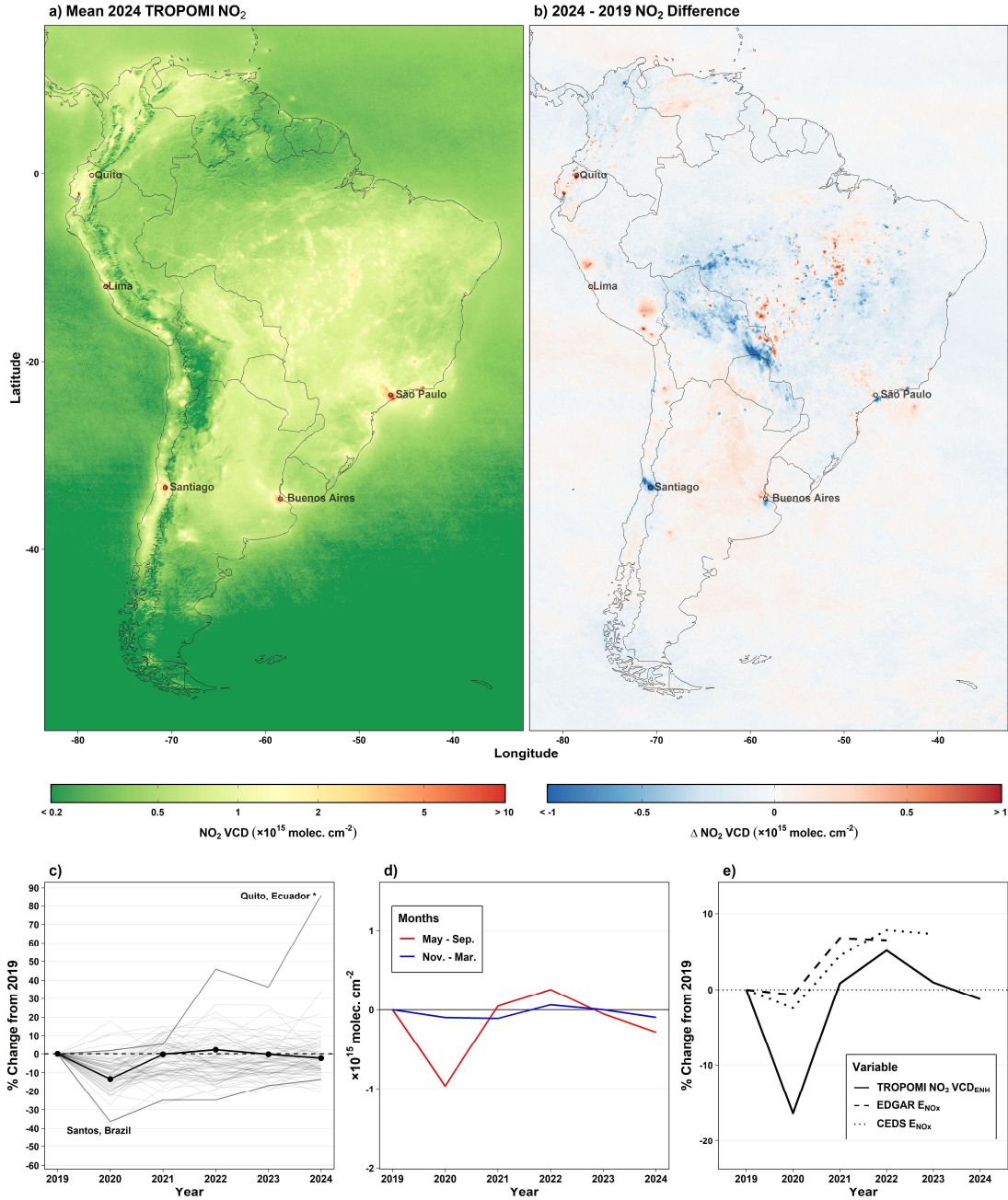
### 413 5.5 South America

414 The largest 2024 mean VCDs in South America are observed in urban regions, including near Lima, Peru ( $6.3 \times 10^{15}$  molecules  
415 cm<sup>-2</sup>); Santiago, Chile ( $9.7 \times 10^{15}$  molecules cm<sup>-2</sup>); and Sao Paulo, Brazil ( $7.3 \times 10^{15}$  molecules cm<sup>-2</sup>) (Fig. 11a). Regions near  
416 Santiago experienced some of the largest differences in VCD in South America between 2019 and 2024 (Fig. 11b) ( $-2.2 \times 10^{15}$   
417 molecules cm<sup>-2</sup>), while Quito, Ecuador experienced a significant increase for that period ( $+12.7 \pm 1.9\%$  yr<sup>-1</sup>;  $p < 0.001$ ).

418 South American cities experienced a 10% population-weighted VCD decrease in 2020, with mean concentrations rebounding  
419 to 2019 values by 2021 and remaining around those levels through 2024 (Fig. 11ce). One notable exception is Quito, Ecuador,  
420 which experienced a VCD increase of over 85% through 2024. Santos, Brazil, an active port town southeast of São Paulo,  
421 experienced one of the largest VCD decreases in South America, with a 35% decrease in VCDs from 2019 to 2020, followed  
422 by sustained, gradual annual increases through 2024.

423 Seasonal changes impacted South American cities less than cities on other continents through 2024 (Fig. 11d), with mean  
424 winter and summer VCDs both changing by less than  $0.3 \times 10^{15}$  molecules cm<sup>-2</sup> through 2024. Accounting for urban  
425 background concentrations, South American cities experienced a population-weighted VCD<sub>ENH</sub> decrease of 16% from 2019 to  
426 2020, with concentrations rebounding to near 2019 levels by 2021 (Fig. 11e). Both EDGAR and CEDS estimated similar  
427 relative population-weighted NO<sub>x</sub> emission changes for the region, though neither inventory appeared to capture the robust  
428 2020 decrease observed by TROPOMI (Fig. 11e). Both inventories experienced a similar mean difference between emissions

429 and  $VCD_{ENH}$  (+7.7% and +6.7%, respectively), suggesting that urban  $NO_x$  emissions in both inventories may be overestimated  
 430 for the region.



431

432 **Figure 11: Same as Fig. 6, but for South America.**

## 433 6 TROPOMI NO<sub>2</sub> VCD Changes in Oil, Gas and Other Mining Regions

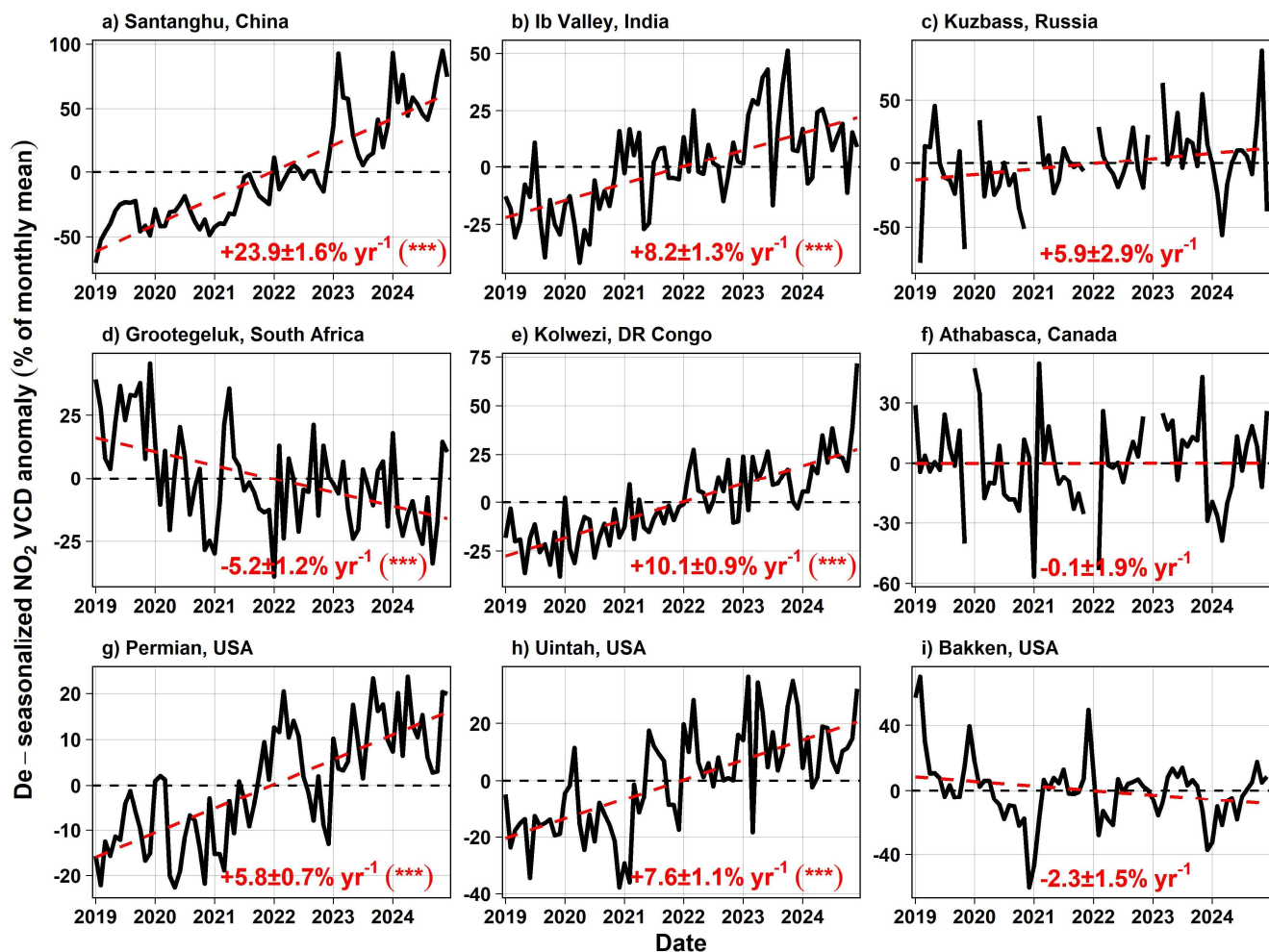
434 NO<sub>2</sub> can be readily observed over oil, gas, and other mining regions due to emissions from drilling and extraction equipment,  
435 processing plants, compressors, truck traffic, and routine or episodic flaring. In these settings, increases or decreases in NO<sub>2</sub>  
436 can signify shifts in production levels or changes in mining activity. Because NO<sub>2</sub> responds quickly to changes in combustion-  
437 related activity, satellite retrievals serve as an effective proxy for monitoring relative operational intensity in major extraction  
438 regions (Dix et al., 2022).

439 Known coal-dominated mining regions showed pronounced NO<sub>2</sub> VCD increases from 2019 to 2024 (Fig. 12). The sparsely-  
440 populated Santanghu Basin (Fig. 12a), a region in eastern Xinjiang Province with a relatively nascent coal mining industry  
441 (Zhang et al., 2018; Liu et al., 2018), represented the most substantial increase in VCD over China through 2024 ( $23.9 \pm 1.6\%$   
442  $\text{yr}^{-1}$ ;  $p < 0.001$ ). The recent expansion of mining operations is evident in visible satellite imagery (Fig. S20). The largest regional  
443 increase in VCD anywhere in India from 2019 to 2024 ( $+2.1 \times 10^{15}$  molecules  $\text{cm}^{-2}$ ) was observed in the Ib Valley in  
444 northwestern Odisha state (Fig. 12b). The region contains multiple surface coal mines and coal-fired power plants (Varma et  
445 al., 2015), with VCDs increasing at a rate of  $8.2 \pm 1.3\% \text{ yr}^{-1}$  ( $p < 0.001$ ). NO<sub>2</sub> VCDs near numerous other coal mines and power  
446 plants throughout India exhibited changes, but NO<sub>2</sub> VCD increases were more prevalent than decreases. In the Kuzbass Region  
447 of Siberia, one of Russia's largest coal mining regions, 2024 annual mean VCDs were  $2.4 \times 10^{15}$  molecules  $\text{cm}^{-2}$  higher than  
448 in 2019, though annual changes were not statistically significant (Fig. 12c). A previous study identified a correlation between  
449 space-based NO<sub>2</sub> observations and regional coal production in the Kuzbass region (Labzovskii et al., 2022), providing relevant  
450 context for the observed VCD changes. Increased VCDs were also observed over rare earth metal mines. In a mining region  
451 known as the Copperbelt in the south of the Democratic Republic of the Congo (DRC), broad NO<sub>2</sub> VCD increases were  
452 observed, including at a large surface copper and cobalt mine near the city of Kolwezi (Fig. 12e). VCDs at the Kolwezi mine  
453 increased at a rate of  $10.1 \pm 0.9\% \text{ yr}^{-1}$  ( $p < 0.001$ ) from 2019 to 2024. Numerous surface mines exist in the region, with most  
454 observing increases in NO<sub>x</sub> emissions from mining operations in recent years (Martínez-Alonso et al., 2023).

455 Not all coal regions experienced increased VCDs. Northwest of Johannesburg, South Africa in Limpopo Province, NO<sub>2</sub> VCDs  
456 near the Grootegeluk surface coal mine, together with two adjacent power plants (Faure et al., 2010; Shikwambana et al., 2020)  
457 decreased at a rate of  $-5.2 \pm 1.2\% \text{ yr}^{-1}$  ( $p < 0.001$ ) from 2019 to 2024 (Fig. 12d). The region represented one of the largest NO<sub>2</sub>  
458 signatures in Africa in 2024, despite the significant decrease for this period (Fig. 8a).

459 Oil and gas extraction areas in North America experienced diverse patterns. Annual mean NO<sub>2</sub> VCDs at the Athabasca oil  
460 sands in Alberta, Canada were slightly lower in 2024 than in 2019, although the decrease for the period was insignificant ( $p >$   
461  $0.05$ ; Fig. 12f). The Bakken region in North Dakota, U.S. experienced a similarly insignificant decrease in VCDs (Fig. 12i).  
462 Notable increases occurred in the Permian (Fig. 12g) and Uintah (Fig. 12h) Basins in the southwestern U.S. experiencing  
463 significant increases of  $5.8 \pm 0.7\% \text{ yr}^{-1}$  ( $p < 0.001$ ) and  $7.6 \pm 1.1\% \text{ yr}^{-1}$  ( $p < 0.001$ ), respectively.

464



465

466 **Figure 12: Monthly time series of de-seasonalized NO<sub>2</sub> VCDs over selected oil, gas, and other mining regions. Black lines denote de-**  
 467 **seasonalized VCDs, and dashed red lines represent ordinary least-squares regression for each site. Months with missing data lacked**  
 468 **quality-assured TROPOMI observations. The % change yr<sup>-1</sup>, standard error and statistical significance is reported each panel. Note**  
 469 **the differing y-axis extents for each panel.**

## 470 7 Conclusions

471 We present a global analysis of urban TROPOMI tropospheric NO<sub>2</sub> VCD from 2019 to 2024 using GHS-SMOD-defined urban  
 472 boundaries, encompassing more than 11,500 cities. Our results reveal statistically lower urban population-weighted NO<sub>2</sub> VCDs  
 473 in 2024 than in 2019 in Asia and Oceania (-17%) and Europe (-13%) with particularly strong reductions in cities including  
 474 Seoul (-9.4 ± 1.0% yr<sup>-1</sup>; p < 0.001), Guangzhou (-5.6 ± 1.3% yr<sup>-1</sup>; p < 0.001), and London, England (-5.4 ± 1.3% yr<sup>-1</sup>; p < 0.001).  
 475 These decreases generally reflect a combination of long-term emissions control policies and economic incentives, indicating  
 476 policies to tackle NO<sub>2</sub> pollution have broadly worked. COVID-19 induced reductions in activity often caused a temporary NO<sub>2</sub>  
 477 reduction but is unlikely to have caused much of the long-term changes between 2019 and 2024. Conversely, urban NO<sub>2</sub> in

478 numerous African cities have increased over the same period, with Abidjan ( $+6.6 \pm 1.2\% \text{ yr}^{-1}$ ;  $p < 0.001$ ), Cairo ( $+2.3 \pm 0.8\% \text{ yr}^{-1}$ ;  $p = 0.006$ ) and Addis Ababa ( $+2.4 \pm 1.1\% \text{ yr}^{-1}$ ;  $p = 0.012$ ) representing larger cities that are leading the continent's upward  
479 tendency. Though numerous populous North American cities exhibited significant VCD decreases, population-weighted urban  
480 levels for the continent as a whole did not show a significant change. Similarly, South American cities exhibited an insignificant  
481 VCD change from 2019 to 2024, apart from May-September in 2020. Population-weighted  $\text{NO}_2$  VCDs increases were most  
482 notable in countries in the Middle East and Africa, highlighting a potential degradation in air quality in regions of the world  
483 that lack extensive ground-level monitoring.

485 Evaluating annual changes in TROPOMI  $\text{NO}_2$  urban enhancements ( $\text{VCD}_{\text{ENH}}$ )—the difference between mean urban and  
486 background VCDs—against changes in EDGAR and CEDS  $\text{NO}_x$  emissions inventories, we highlight potential discrepancies  
487 in inventory estimates in urban regions. In African, Asian and European cities, changes in  $\text{VCD}_{\text{ENH}}$  tend to exceed changes in  
488 both EDGAR and CEDS emissions, pointing to potential inventory overestimates in  $\text{NO}_x$  emissions. In North America,  
489 EDGAR agrees well with  $\text{VCD}_{\text{ENH}}$  (mean difference of 0.3% relative to 2019 values), while CEDS  $\text{NO}_x$  emissions are 6.1%  
490 lower than  $\text{VCD}_{\text{ENH}}$ , relative to their respective 2019 values. These mismatches may stem from rapidly evolving emission  
491 sources or limitations in the EDGAR and CEDS bottom-up inventory methods. Similar discrepancies in emissions inventories  
492 in the Global South have been reported in previous studies (Ahn et al., 2023), suggesting larger emissions uncertainties in  
493 regions where unmonitored emissions activity may be significant.

494 In most regions, VCD changes from 2019 to 2024 were driven by changes during the colder months (November – March).  
495 This was most pronounced in Asian cities, where mean cold season VCDs decreased by  $-1.2 \times 10^{15} \text{ molecules cm}^{-2}$  (-18%)  
496 from 2019 to 2024, compared with warm season VCD decreases of  $-0.5 \times 10^{15} \text{ molecules cm}^{-2}$  (-13%). Large changes in  $\text{NO}_2$   
497 were not confined to urban regions alone. We identified localized increases near fossil fuel and other mining operations,  
498 including in the Santanghu Basin in China ( $+23.9 \pm 1.6\% \text{ yr}^{-1}$ ;  $p < 0.001$ ), the Permian ( $+5.8 \pm 0.7\% \text{ yr}^{-1}$ ;  $p < 0.001$ ) and Uintah  
499 ( $+7.6 \pm 1.1\% \text{ yr}^{-1}$ ;  $p < 0.001$ ) Basins in the U.S., and the Copperbelt region of the DRC ( $10.1 \pm 0.9\% \text{ yr}^{-1}$ ;  $p < 0.001$ ), signaling  
500 expanding industrial activity. In Khartoum and Kyiv, conflict and displacement drove sharp reductions in  $\text{NO}_2$ , demonstrating  
501 the utility of satellite data in detecting societal disruptions.

502 Several limitations of this work should be noted. First, satellite  $\text{NO}_2$  column densities may not always reflect surface-level  $\text{NO}_2$   
503 concentrations, particularly in regions with vertically elevated sources. In urban areas dominated by surface-based  
504 transportation emissions,  $\text{NO}_2$  VCDs are likely more representative of surface exposure. However, in areas with tall-stack  
505 sources, such as power plants,  $\text{NO}_2$  columns may be decoupled from near-surface levels (Brett et al., 2025). Second, we assume  
506 static city boundaries defined by the 2023 version of GHS-SMOD, with population estimates from 2020. This is likely a  
507 reasonable approximation for urbanized regions in Europe and North America, where built-up area changes are slow, but may  
508 introduce uncertainty in rapidly urbanizing regions of Africa and Asia over a six-year period. Future analyses could incorporate  
509 time-varying urban boundaries to address this. Additionally, while many of the changes presented here reflect variability in  
510 anthropogenic  $\text{NO}_x$  emissions, it is important to recognize that atmospheric chemistry also influences the observed  $\text{NO}_2$

511 variability. Seasonal differences in photochemical lifetimes (i.e., longest in winter), boundary layer mixing (i.e., more vertical  
512 mixing in summer), chemical partitioning between NO and NO<sub>2</sub>, meteorological variability, and contributions from additional  
513 emissions sources including soil NO<sub>x</sub> and fire emissions, can all modulate the magnitude and timing of observed NO<sub>2</sub>  
514 concentrations. These processes likely contribute to some of the regional and seasonal differences highlighted in this study.

515 Taken together, these results demonstrate the utility of high-resolution satellite instruments for characterizing both broad  
516 regional NO<sub>2</sub> signals and localized changes, and linking with anthropogenically induced factors such as urban growth,  
517 industrial expansion, policy interventions, and conflict. This highlights potential in using TROPOMI observations as an  
518 accountability agent to determine how local changes in human activities affect local and global air pollution. As the TROPOMI  
519 record lengthens and newer, geostationary satellites come online and begin to detect changes in atmospheric composition,  
520 continued space-based monitoring will be essential for improving our understanding of atmospheric composition and chemistry  
521 around the globe.

#### 522 **Data Availability.**

523 The level 3 annual and monthly average TROPOMI NO<sub>2</sub> VCDs are available at 10.5067/ACADNS5UBWPQ and  
524 <https://doi.org/10.5067/KKPPL39PEIGE>, respectively. The GHS-SMOD urban boundaries can be downloaded from  
525 <https://human-settlement.emergency.copernicus.eu/download.php?ds=smod>. The EDGARv8.1 NO<sub>x</sub> emissions can be  
526 downloaded from [https://edgar.jrc.ec.europa.eu/dataset\\_ap81](https://edgar.jrc.ec.europa.eu/dataset_ap81). The CEDS NO<sub>x</sub> emissions can be downloaded from  
527 <https://aims2.llnl.gov/>. Annual and monthly mean TROPOMI NO<sub>2</sub> VCDs for each GHS-SMOD urban cluster can be found at  
528 <https://doi.org/10.5281/zenodo.18665781>.

#### 529 **Supplement.**

530 The supplement contains additional figures related to the study, including: S1 Background NO<sub>2</sub> sensitivity in Beijing. S2  
531 Background NO<sub>2</sub> sensitivity in Los Angeles. S3 Background NO<sub>2</sub> sensitivity in London. S4 Background NO<sub>2</sub> sensitivity in  
532 Moscow. S5 Annual background NO<sub>2</sub> changes by continent. S6 Relative NO<sub>2</sub> VCD<sub>ENH</sub> changes by continent. S7 Background  
533 NO<sub>2</sub> for adjacent cities. S8 GHS-SMOD urban clusters example. S9 Data disaggregation example. S10 Khartoum NO<sub>2</sub> time  
534 series. S11 NO<sub>2</sub> increases in three global cities. S12 Annual mean NO<sub>2</sub> in Tehran, Iran. S13 Annual mean NO<sub>2</sub> VCDs for  
535 Bangladeshi cities. S14 Seasonal relative NO<sub>2</sub> changes by continent. S15 Annual mean NO<sub>2</sub> changes in the European Union.  
536 S16 Annual mean NO<sub>2</sub> changes in Russian and Ukrainian cities. S17 Seasonal NO<sub>2</sub> changes by continent, without Russia. S18  
537 NO<sub>2</sub> increases in three U.S. cities. S19 Satellite view of surface mines.

538 **Author Contribution.**

539 D.H. and D.G. contributed to the project design. D.G. processed and provided the annually- and monthly-averaged NO<sub>2</sub> vertical  
540 column densities. All authors edited the manuscript.

541 **Competing Interests.**

542 The authors declare that they have no conflict of interest.

543 **Acknowledgements.**

544 This work was supported by National Aeronautics and Space Administration (NASA) Health and Air Quality Applied Sciences  
545 Team (HAQAST) grant #80NSSC21K0511 and NASA Aura Atmospheric Composition Modeling and Analysis Program  
546 (ACMAP) grant #80NSSC23K1002.

547

548 **References**

549 Ahn, D. Y., Goldberg, D. L., Coombes, T., Kleiman, G., and Anenberg, S. C.: CO<sub>2</sub> emissions from C40 cities: citywide  
550 emission inventories and comparisons with global gridded emission datasets, *Environmental Research Letters*, 18, 034032,  
551 <https://doi.org/10.1088/1748-9326/ACBB91>, 2023.

552 Anenberg, S. C., Mohegh, A., Goldberg, D. L., Kerr, G. H., Brauer, M., Burkart, K., Hystad, P., Larkin, A., Wozniak, S., and  
553 Lamsal, L.: Long-term trends in urban NO<sub>2</sub> concentrations and associated paediatric asthma incidence: estimates from  
554 global datasets, *Lancet Planet Health*, 6, e49–e58, [https://doi.org/10.1016/S2542-5196\(21\)00255-](https://doi.org/10.1016/S2542-5196(21)00255-2/ATTACHMENT/7B9BB37F-5DEA-41D7-A9CC-9AFFA3989D6A/MMC1.PDF)  
555 [2/ATTACHMENT/7B9BB37F-5DEA-41D7-A9CC-9AFFA3989D6A/MMC1.PDF](https://doi.org/10.1016/S2542-5196(21)00255-2/ATTACHMENT/7B9BB37F-5DEA-41D7-A9CC-9AFFA3989D6A/MMC1.PDF), 2022.

556 Bovensmann, H., Burrows, J. P., Buchwitz, M., Frerick, J., Noël, S., Rozanov, V. V., Chance, K. V., and Goede, A. P. H.:  
557 SCIAMACHY: Mission Objectives and Measurement Modes, *J Atmos Sci*, 56, 127–150, [https://doi.org/10.1175/1520-](https://doi.org/10.1175/1520-0469(1999)056<0127:SMOAMM>2.0.CO;2)  
558 [0469\(1999\)056<0127:SMOAMM>2.0.CO;2](https://doi.org/10.1175/1520-0469(1999)056<0127:SMOAMM>2.0.CO;2), 1999.

559 Brett, N., Arnold, S. R., Law, K. S., Raut, J.-C., Onishi, T., Barret, B., Dieudonné, E., Cesler-Maloney, M., Simpson, W.,  
560 Bekki, S., Savarino, J., Albertin, S., Gilliam, R., Fahey, K., Pouliot, G., Huff, D., and D’Anna, B.: Estimating Power Plant  
561 Contributions to Surface Pollution in a Wintertime Arctic Environment, *ACS ES&T Air*, 2, 943–956,  
562 <https://doi.org/10.1021/ACSESTAIR.5C00030>, 2025.

563 Burrows, J. P., Weber, M., Buchwitz, M., Rozanov, V., Ladstätter-Weißmayer, A., Richter, A., Debeek, R., Hoogen, R.,  
564 Bramstedt, K., Eichmann, K. U., Eisinger, M., and Perner, D.: The Global Ozone Monitoring Experiment (GOME):

565 Mission Concept and First Scientific Results, *J Atmos Sci*, 56, 151–175, <https://doi.org/10.1175/1520->  
566 0469(1999)056<0151:TGOMEG>2.0.CO;2, 1999.

567 Castellanos, P., Boersma, K. F., and Van Der Werf, G. R.: Satellite observations indicate substantial spatiotemporal variability  
568 in biomass burning NO<sub>x</sub> emission factors for South America, *Atmos Chem Phys*, 14, 3929–3943,  
569 <https://doi.org/10.5194/ACP-14-3929-2014>, 2014.

570 Chen, X., Qi, L., Li, S., and Duan, X.: Long-term NO<sub>2</sub> exposure and mortality: A comprehensive meta-analysis, *Environmental*  
571 *Pollution*, 341, 122971, <https://doi.org/10.1016/J.ENVPOL.2023.122971>, 2024.

572 Cifuentes-Faura, J.: European Union policies and their role in combating climate change over the years, *Air Qual Atmos*  
573 *Health*, 15, 1333–1340, <https://doi.org/10.1007/S11869-022-01156-5/FIGURES/1>, 2022.

574 Cooper, M. J., Martin, R. V., Hammer, M. S., Levelt, P. F., Veefkind, P., Lamsal, L. N., Krotkov, N. A., Brook, J. R., and  
575 McLinden, C. A.: Global fine-scale changes in ambient NO<sub>2</sub> during COVID-19 lockdowns, *Nature* 2022 601:7893, 601,  
576 380–387, <https://doi.org/10.1038/s41586-021-04229-0>, 2022.

577 Crippa, M., Guizzardi, D., Muntean, M., Schaaf, E., Dentener, F., Van Aardenne, J. A., Monni, S., Doering, U., Olivier, J. G.  
578 J., Pagliari, V., and Janssens-Maenhout, G.: Gridded emissions of air pollutants for the period 1970–2012 within EDGAR  
579 v4.3.2, *Earth Syst Sci Data*, 10, 1987–2013, <https://doi.org/10.5194/ESSD-10-1987-2018>, 2018.

580 Crippa, M., Guizzardi, D., Pagani, F., Schiavina, M., Melchiorri, M., Pisoni, E., Graziosi, F., Muntean, M., Maes, J., Dijkstra,  
581 L., Damme, M. Van, Clarisse, L., and Coheur, P.: Insights into the spatial distribution of global, national, and subnational  
582 greenhouse gas emissions in the Emissions Database for Global Atmospheric Research (EDGAR v8.0), *Earth Syst. Sci.*  
583 *Data*, 16, 2811–2830, <https://doi.org/10.5194/essd-16-2811-2024>, 2024.

584 Cui, R. Y., Hultman, N., Cui, D., McJeon, H., Yu, S., Edwards, M. R., Sen, A., Song, K., Bowman, C., Clarke, L., Kang, J.,  
585 Lou, J., Yang, F., Yuan, J., Zhang, W., and Zhu, M.: A plant-by-plant strategy for high-ambition coal power phaseout in  
586 China, *Nature Communications* 2021 12:1, 12, 1–10, <https://doi.org/10.1038/s41467-021-21786-0>, 2021.

587 Dang, R., Jacob, D. J., Shah, V., Eastham, S. D., Fritz, T. M., Mickley, L. J., Liu, T., Wang, Y., and Wang, J.: Background  
588 nitrogen dioxide (NO<sub>2</sub>) over the United States and its implications for satellite observations and trends: effects of nitrate  
589 photolysis, aircraft, and open fires, *Atmos Chem Phys*, 23, 6271–6284, <https://doi.org/10.5194/ACP-23-6271-2023>, 2023.

590 Dix, B., de Bruin, J., Roosenbrand, E., Vlemmix, T., Francoeur, C., Gorchov-Negron, A., McDonald, B., Zhizhin, M., Elvidge,  
591 C., Veefkind, P., Levelt, P., and de Gouw, J.: Nitrogen Oxide Emissions from U.S. Oil and Gas Production: Recent Trends  
592 and Source Attribution, *Geophys Res Lett*, 47, e2019GL085866, <https://doi.org/10.1029/2019GL085866>, 2020.

593 Dix, B., Francoeur, C., Li, M., Serrano-Calvo, R., Levelt, P. F., Veefkind, J. P., McDonald, B. C., and de Gouw, J.: Quantifying  
594 NO<sub>x</sub> Emissions from U.S. Oil and Gas Production Regions Using TROPOMI NO<sub>2</sub>, *ACS Earth Space Chem*, 6, 403–414,

595 [https://doi.org/10.1021/ACSEARTHSPACECHEM.1C00387/ASSET/IMAGES/LARGE/SP1C00387\\_0008.JPEG](https://doi.org/10.1021/ACSEARTHSPACECHEM.1C00387/ASSET/IMAGES/LARGE/SP1C00387_0008.JPEG),  
596 2022.

597 Duncan, B. N., Lamsal, L. N., Thompson, A. M., Yoshida, Y., Lu, Z., Streets, D. G., Hurwitz, M. M., and Pickering, K. E.: A  
598 space-based, high-resolution view of notable changes in urban NO<sub>x</sub> pollution around the world (2005–2014), *J Geophys*  
599 *Res*, 121, 976–996, <https://doi.org/10.1002/2015JD024121>, 2016.

600 Faure, K., Willis, J. P., and Dreyer, J. C.: The grootegeeluk formation in the Waterberg Coalfield, South Africa: facies,  
601 palaeoenvironment and thermal history — evidence from organic and clastic matter, *Int J Coal Geol*, 29, 147–186,  
602 [https://doi.org/10.1016/0166-5162\(95\)00029-1](https://doi.org/10.1016/0166-5162(95)00029-1), 1996.

603 Fioletov, V., McLinden, C. A., Griffin, D., Krotkov, N., Liu, F., and Eskes, H.: Quantifying urban, industrial, and background  
604 changes in NO<sub>2</sub> during the COVID-19 lockdown period based on TROPOMI satellite observations, *Atmos. Chem. Phys.*,  
605 22, 4201–4236, <https://doi.org/10.5194/acp-22-4201-2022>, 2022.

606 Fioletov, V., McLinden, C. A., Griffin, D., Zhao, X., and Eskes, H.: Global seasonal urban, industrial, and background NO<sub>2</sub>  
607 estimated from TROPOMI satellite observations, *Atmos. Chem. Phys.*, 25, 575–596, <https://doi.org/10.5194/acp-25-575->  
608 2025, 2025.

609 Fisher, B. L., Lamsal, L. N., Fasnacht, Z., Oman, L. D., Joiner, J., Krotkov, N. A., Choi, S., Qin, W., and Yang, E. S.: Revised  
610 estimates of NO<sub>2</sub> reductions during the COVID-19 lockdowns using updated TROPOMI NO<sub>2</sub> retrievals and model  
611 simulations, *Atmos Environ*, 326, 120459, <https://doi.org/10.1016/J.ATMOSENV.2024.120459>, 2024.

612 Fishman, J., Iraci, L. T., Al-Saadi, J., Chance, K., Chavez, F., Chin, M., Coble, P., Davis, C., DiGiacomo, P. M., Edwards, D.,  
613 Eldering, A., Goes, J., Herman, J., Hu, C., Jacob, D. J., Jordan, C., Kawa, S. R., Key, R., Liu, X., Lohrenz, S., Mannino,  
614 A., Natraj, V., Neil, D., Neu, J., Newchurch, M., Pickering, K., Salisbury, J., Sosik, H., Subramaniam, A., Tzortziou, M.,  
615 Wang, J., and Wang, M.: The United States’ Next Generation of Atmospheric Composition and Coastal Ecosystem  
616 Measurements: NASA’s Geostationary Coastal and Air Pollution Events (GEO-CAPE) Mission, *Bull Am Meteorol Soc*,  
617 93, 1547–1566, <https://doi.org/10.1175/BAMS-D-11-00201.1>, 2012.

618 De Foy, B., Lu, Z., and Streets, D. G.: Satellite NO<sub>2</sub> retrievals suggest China has exceeded its NO<sub>x</sub> reduction goals from the  
619 twelfth Five-Year Plan, *Scientific Reports* 2016 6:1, 6, 1–9, <https://doi.org/10.1038/srep35912>, 2016.

620 Geddes, J. A., Martin, R. V., Boys, B. L., and van Donkelaar, A.: Long-term trends worldwide in ambient NO<sub>2</sub> concentrations  
621 inferred from satellite observations, *Environ Health Perspect*, 124, 281–289,  
622 [https://doi.org/10.1289/EHP.1409567/SUPPL\\_FILE/EHP.1409567.S001.ACCO.PDF](https://doi.org/10.1289/EHP.1409567/SUPPL_FILE/EHP.1409567.S001.ACCO.PDF), 2016.

623 Van Geffen, J., Eskes, H., Compernelle, S., Pinardi, G., Verhoelst, T., Lambert, J.-C., Sneep, M., Linden, M. Ter, Ludewig,  
624 A., Folkert Boersma, K., and Pepijn Veeffkind, J.: Sentinel-5P TROPOMI NO<sub>2</sub> retrieval: impact of version v2.2

625 improvements and comparisons with OMI and ground-based data, *Atmos. Meas. Tech*, 15, 2037–2060,  
626 <https://doi.org/10.5194/amt-15-2037-2022>, 2022.

627 Ghude, S. D., Karumuri, R. K., Jena, C., Kulkarni, R., Pfister, G. G., Sajjan, V. S., Pithani, P., Debnath, S., Kumar, R., Upendra,  
628 B., Kulkarni, S. H., Lal, D. M., Vander A, R. J., and Mahajan, A. S.: What is driving the diurnal variation in tropospheric  
629 NO<sub>2</sub> columns over a cluster of high emission thermal power plants in India?, *Atmos Environ X*, 5, 100058,  
630 <https://doi.org/10.1016/J.AEAOA.2019.100058>, 2020.

631 Glissenaar, I., Boersma, K. F., Anglou, I., Rijdsdijk, P., Verhoelst, T., Compernelle, S., Pinardi, G., Lambert, J.-C., Van  
632 Roozendaal, M., and Eskes, H.: TROPOMI Level 3 tropospheric NO<sub>2</sub> dataset with advanced uncertainty analysis from  
633 the ESA CCI+ ECV precursor project, *Earth Syst Sci Data*, 17, 4627–4650, <https://doi.org/10.5194/ESSD-17-4627-2025>,  
634 2025.

635 Goldberg, D.: HAQAST Sentinel-5P TROPOMI Nitrogen Dioxide (NO<sub>2</sub>) GLOBAL Monthly Level 3 0.1 x 0.1 Degree  
636 Gridded Data Version 2.4 (HAQ\_TROPOMI\_NO2\_GLOBAL\_M\_L3) at GES DISC,  
637 <https://doi.org/10.5067/KKPPL39PEIGE>, 15 March 2024.

638 Goldberg, D. L., Anenberg, S. C., Kerr, G. H., Mohegh, A., Lu, Z., and Streets, D. G.: TROPOMI NO<sub>2</sub> in the United States:  
639 A Detailed Look at the Annual Averages, Weekly Cycles, Effects of Temperature, and Correlation With Surface NO<sub>2</sub>  
640 Concentrations, *Earths Future*, 9, <https://doi.org/10.1029/2020EF001665>, 2021a.

641 Goldberg, D. L., Anenberg, S. C., Lu, Z., Streets, D. G., Lamsal, L. N., E McDuffie, E., and Smith, S. J.: Urban NO<sub>x</sub> emissions  
642 around the world declined faster than anticipated between 2005 and 2019, *Environmental Research Letters*, 16, 115004,  
643 <https://doi.org/10.1088/1748-9326/AC2C34>, 2021b.

644 Goldberg, D. L., Tao, M., Kerr, G. H., Ma, S., Tong, D. Q., Fiore, A. M., Dickens, A. F., Adelman, Z. E., and Anenberg, S.  
645 C.: Evaluating the spatial patterns of U.S. urban NO<sub>x</sub> emissions using TROPOMI NO<sub>2</sub>, *Remote Sens Environ*, 300,  
646 <https://doi.org/10.1016/j.rse.2023.113917>, 2024.

647 de Gouw, J. A., Veeffkind, J. P., Roosenbrand, E., Dix, B., Lin, J. C., Landgraf, J., and Levelt, P. F.: Daily Satellite Observations  
648 of Methane from Oil and Gas Production Regions in the United States, *Sci Rep*, 10, 1–10, [https://doi.org/10.1038/S41598-](https://doi.org/10.1038/S41598-020-57678-4)  
649 [020-57678-4](https://doi.org/10.1038/S41598-020-57678-4);TECHMETA=134;SUBJMETA=106,169,172,35,704,824;KWRD=ATMOSPHERIC+CHEMISTRY,  
650 2020.

651 Guo, Z., Abushama, H., Siddig, K., Kirui, O. K., Abay, K., and You, L.: Monitoring Indicators of Economic Activities in  
652 Sudan Amidst Ongoing Conflict Using Satellite Data, *Defence and Peace Economics*,  
653 <https://doi.org/10.1080/10242694.2023.2290474>;PAGE:STRING:ARTICLE/CHAPTER, 2023.

654 Hajmohammadi, H. and Heydecker, B.: Evaluation of air quality effects of the London ultra-low emission zone by state-space  
655 modelling, *Atmos Pollut Res*, 13, 101514, <https://doi.org/10.1016/J.APR.2022.101514>, 2022.

656 Harake, W., Jamali, I., and Abou Hamde, N.: Lebanon Economic Monitor : Lebanon Sinking (to the Top 3), Washington, D.C.,  
657 <https://doi.org/http://documents.worldbank.org/curated/en/394741622469174252>, 2021.

658 Herman, J., Cede, A., Spinei, E., Mount, G., Tzortziou, M., and Abuhassan, N.: NO<sub>2</sub> column amounts from ground-based  
659 Pandora and MFDOAS spectrometers using the direct-sun DOAS technique: Intercomparisons and application to OMI  
660 validation, *Journal of Geophysical Research: Atmospheres*, 114, <https://doi.org/10.1029/2009JD011848>, 2009.

661 Hersbach, H., Bell, B., Berrisford, P., Hirahara, S., Horányi, A., Muñoz-Sabater, J., Nicolas, J., Peubey, C., Radu, R., Schepers,  
662 D., Simmons, A., Soci, C., Abdalla, S., Abellan, X., Balsamo, G., Bechtold, P., Biavati, G., Bidlot, J., Bonavita, M., De  
663 Chiara, G., Dahlgren, P., Dee, D., Diamantakis, M., Dragani, R., Flemming, J., Forbes, R., Fuentes, M., Geer, A.,  
664 Haimberger, L., Healy, S., Hogan, R. J., Hólm, E., Janisková, M., Keeley, S., Laloyaux, P., Lopez, P., Lupu, C., Radnoti,  
665 G., de Rosnay, P., Rozum, I., Vamborg, F., Villaume, S., and Thépaut, J. N.: The ERA5 global reanalysis, *Quarterly  
666 Journal of the Royal Meteorological Society*, 146, 1999–2049, <https://doi.org/10.1002/QJ.3803>, 2020.

667 Hilboll, A., Richter, A., and Burrows, J. P.: Sciences ess Atmospheric Chemistry and Physics Climate of the Past Geoscientific  
668 Instrumentation Methods and Data Systems Long-term changes of tropospheric NO<sub>2</sub> over megacities derived from  
669 multiple satellite instruments, *Atmos. Chem. Phys*, 13, 4145–4169, <https://doi.org/10.5194/acp-13-4145-2013>, 2013.

670 Ho, C. H., Heo, J. W., Chang, M., Choi, W., Kim, J., Kim, S. W., and Oh, H. R.: Regulatory measures significantly reduced  
671 air-pollutant concentrations in Seoul, Korea, *Atmos Pollut Res*, 12, 101098, <https://doi.org/10.1016/J.APR.2021.101098>,  
672 2021.

673 Hoesly, R. M., Smith, S. J., Ahsan, H., Prime, N., O'Rourke, P., Crippa, M., Klimont, Z., Guizzardi, D., Feng, L., Harkins, C.,  
674 McDonald, B. C., & Wang, S: *CEDS v\_2025\_04\_18 Gridded Data 0.1 degree*. Zenodo.  
675 <https://doi.org/10.5281/zenodo.15001545>, 2025.

676 Huber, D. E., Kort, E. A., and Steiner, A. L.: Soil Moisture, Soil NO<sub>x</sub> and Regional Air Quality in the Agricultural Central  
677 United States, *Journal of Geophysical Research: Atmospheres*, 129, e2024JD041015,  
678 <https://doi.org/10.1029/2024JD041015>, 2024.

679 Jiang, Z., McDonald, B. C., Worden, H., Worden, J. R., Miyazaki, K., Qu, Z., Henze, D. K., Jones, D. B. A., Arellano, A. F.,  
680 Fischer, E. V., Zhu, L., and Folkert Boersma, K.: Unexpected slowdown of US pollutant emission reduction in the past  
681 decade, *Proc Natl Acad Sci U S A*, 115, 5099–5104, <https://doi.org/10.1073/PNAS.1801191115/-/DCSUPPLEMENTAL>,  
682 2018.

683 Jiang, Z., Zhu, R., Miyazaki, K., McDonald, B. C., Klimont, Z., Zheng, B., Boersma, K. F., Zhang, Q., Worden, H., Worden,  
684 J. R., Henze, D. K., Jones, D. B. A., Denier van der Gon, H. A. C., and Eskes, H.: Decadal Variabilities in Tropospheric  
685 Nitrogen Oxides Over United States, Europe, and China, *Journal of Geophysical Research: Atmospheres*, 127,  
686 e2021JD035872, <https://doi.org/10.1029/2021JD035872>, 2022.

687 Jin, X., Zhu, Q., Cohen, R. C., and Xiaomeng, J.: Direct estimates of biomass burning NO<sub>x</sub> emissions and lifetimes using  
688 daily observations from TROPOMI, *Atmos. Chem. Phys.*, 21, 15569–15587, <https://doi.org/10.5194/acp-21-15569-2021>,  
689 2021.

690 Kim, E. J., Holloway, T., Kokandakar, A., Harkey, M., Elkins, S., Goldberg, D. L., and Heck, C.: A Comparison of Regression  
691 Methods for Inferring Near-Surface NO<sub>2</sub> With Satellite Data, *Journal of Geophysical Research: Atmospheres*, 129,  
692 e2024JD040906, <https://doi.org/10.1029/2024JD040906>, 2024.

693 Krotkov, N. A., McLinden, C. A., Li, C., Lamsal, L. N., Celarier, E. A., Marchenko, S. V, Swartz, W. H., Bucsela, E. J., Joiner,  
694 J., Duncan, B. N., Folkert Boersma, K., Pepijn Veefkind, J., Levelt, P. F., Fioletov, V. E., Dickerson, R. R., He, H., Lu,  
695 Z., and Streets, D. G.: Aura OMI observations of regional SO<sub>2</sub> and NO<sub>2</sub> pollution changes from 2005 to 2015, *Atmos.*  
696 *Chem. Phys.*, 16, 4605–4629, <https://doi.org/10.5194/acp-16-4605-2016>, 2016.

697 Labzovskii, L. D., Belikov, D. A., and Damiani, A.: Spaceborne NO<sub>2</sub> observations are sensitive to coal mining and processing  
698 in the largest coal basin of Russia, *Sci Rep*, 12, 1–11, [https://doi.org/10.1038/S41598-022-16850-](https://doi.org/10.1038/S41598-022-16850-8)  
699 [8](https://doi.org/10.1038/S41598-022-16850-8);SUBJMETA=106,172,35,4081,704;KWRD=ATMOSPHERIC+SCIENCE,ENVIRONMENTAL+IMPACT,ENVIRO  
700 NMENTAL+SCIENCES, 2022.

701 Lambert, J.-C.: Quarterly Validation Report of the Copernicus Sentinel-5 Precursor Operational Data Products #28: April 2018  
702 – August 2025, 227 pp., 2025.

703 Lamsal, L. N., Duncan, B. N., Yoshida, Y., Krotkov, N. A., Pickering, K. E., Streets, D. G., and Lu, Z.: U.S. NO<sub>2</sub> trends  
704 (2005–2013): EPA Air Quality System (AQS) data versus improved observations from the Ozone Monitoring Instrument  
705 (OMI), *Atmos Environ*, 110, 130–143, <https://doi.org/10.1016/J.ATMOSENV.2015.03.055>, 2015.

706 Laughner, J. L. and Cohen, R. C.: Direct observation of changing NO<sub>x</sub> lifetime in North American cities, *Science* (1979), 366,  
707 723–727, [https://doi.org/https://doi.org/10.1126/science.aax6832](https://doi.org/10.1126/science.aax6832), 2019.

708 Levelt, P. F., Van Den Oord, G. H. J., Dobber, M. R., Mälkki, A., Visser, H., De Vries, J., Stammes, P., Lundell, J. O. V., and  
709 Saari, H.: The ozone monitoring instrument, *IEEE Transactions on Geoscience and Remote Sensing*, 44, 1093–1100,  
710 <https://doi.org/10.1109/TGRS.2006.872333>, 2006.

711 Levelt, P. F., Stein Zweers, D. C., Aben, I., Bauwens, M., Borsdorff, T., De Smedt, I., Eskes, H. J., Lerot, C., Loyola, D. G.,  
712 Romahn, F., Stavrou, T., Theys, N., Van Roozendaal, M., Veefkind, J. P., and Verhoelst, T.: Air quality impacts of  
713 COVID-19 lockdown measures detected from space using high spatial resolution observations of multiple trace gases  
714 from Sentinel-5P/TROPOMI, *Atmos Chem Phys*, 22, 10319–10351, <https://doi.org/10.5194/ACP-22-10319-2022>, 2022.

715 Li, H., Zheng, B., Lei, Y., Hauglustaine, D., Chen, C., Lin, X., Zhang, Y., Zhang, Q., and He, K.: Trends and drivers of  
716 anthropogenic NO<sub>x</sub> emissions in China since 2020, *Environmental Science and Ecotechnology*, 21, 100425,  
717 <https://doi.org/10.1016/J.ESE.2024.100425>, 2024.

- 718 Liu, B., Fu, X., Bechtel, A., Gross, D., Sachsenhofer, R. F., and Li, X.: Middle Permian environmental changes and shale oil  
719 potential evidenced by high-resolution organic petrology, geochemistry and mineral composition of the sediments in the  
720 Santanghu Basin, Northwest China, *Int J Coal Geol*, 185, 119–137, <https://doi.org/10.1016/J.COAL.2017.11.015>, 2018.
- 721 Liu, F., Zhang, Q., Van Der A, R. J., Zheng, B., Tong, D., Yan, L., Zheng, Y., and He, K.: Recent reduction in NO<sub>x</sub> emissions  
722 over China: synthesis of satellite observations and emission inventories, *Environmental Research Letters*, 11, 114002,  
723 <https://doi.org/10.1088/1748-9326/11/11/114002>, 2016.
- 724 Lonsdale, C. R. and Sun, K.: Nitrogen oxides emissions from selected cities in North America, Europe, and East Asia observed  
725 by the TROPOspheric Monitoring Instrument (TROPOMI) before and after the COVID-19 pandemic, *Atmos. Chem.*  
726 *Phys*, 23, 8727–8748, <https://doi.org/10.5194/acp-23-8727-2023>, 2023.
- 727 Ma, Q., Wang, J., Xiong, M., and Zhu, L.: Air Quality Index (AQI) Did Not Improve during the COVID-19 Lockdown in  
728 Shanghai, China, in 2022, Based on Ground and TROPOMI Observations, *Remote Sens (Basel)*, 15, 1295,  
729 <https://doi.org/10.3390/RS15051295/S1>, 2023.
- 730 Martínez-Alonso, S., Veefkind, J. P., Dix, B., Gaubert, B., Theys, N., Granier, C., Soulié, A., Darras, S., Eskes, H., Tang, W.,  
731 Worden, H., de Gouw, J., and Levelt, P. F.: S-5P/TROPOMI-Derived NO<sub>x</sub> Emissions From Copper/Cobalt Mining and  
732 Other Industrial Activities in the Copperbelt (Democratic Republic of Congo and Zambia), *Geophys Res Lett*, 50,  
733 e2023GL104109, <https://doi.org/10.1029/2023GL104109>, 2023.
- 734 Matthias, V., Quante, M., Arndt, J. A., Badeke, R., Fink, L., Petrik, R., Feldner, J., Schwarzkopf, D., Link, E. M., Ramacher,  
735 M. O. P., and Wedemann, R.: The role of emission reductions and the meteorological situation for air quality  
736 improvements during the COVID-19 lockdown period in central Europe, *Atmos Chem Phys*, 21, 13931–13971,  
737 <https://doi.org/10.5194/ACP-21-13931-2021>, 2021.
- 738 Miyazaki, K., Eskes, H., Sudo, K., Folkert Boersma, K., Bowman, K., and Kanaya, Y.: Decadal changes in global surface NO<sub>x</sub>  
739 emissions from multi-constituent satellite data assimilation, *Atmos Chem Phys*, 17, 807–837,  
740 <https://doi.org/10.5194/ACP-17-807-2017>, 2017.
- 741 Panda, M. R., Tyagi, A., Dhanya, C. T., Verma, A., and Swain, A.: Vulnerability assessment of thermal power plants in India  
742 under water stress conditions, *Energy*, 276, 127553, <https://doi.org/10.1016/J.ENERGY.2023.127553>, 2023.
- 743 Richter, A., Burrows, J. P., Nüß, H., Granier, C., and Niemeier, U.: Increase in tropospheric nitrogen dioxide over China  
744 observed from space, *Nature*, 437, 129–132, <https://doi.org/10.1038/nature04092>, 2005.
- 745 Rokicki, T., Bórawski, P., and Szeberényi, A.: The Impact of the 2020–2022 Crises on EU Countries’ Independence from  
746 Energy Imports, Particularly from Russia, *Energies* 2023, Vol. 16, Page 6629, 16, 6629,  
747 <https://doi.org/10.3390/EN16186629>, 2023.

- 748 Schiavina M., Melchiorri M. & Pesaresi M.: GHS-SMOD R2023A - GHS settlement layers, application of the Degree of  
749 Urbanisation methodology (stage I) to GHS-POP R2023A and GHS-BUILT-S R2023A, multitemporal (1975-2030).  
750 European Commission, Joint Research Centre (JRC). [https://doi.org/10.2905/A0DF7A6F-49DE-46EA-9BDE-](https://doi.org/10.2905/A0DF7A6F-49DE-46EA-9BDE-563437A6E2BA)  
751 [563437A6E2BA](https://doi.org/10.2905/A0DF7A6F-49DE-46EA-9BDE-563437A6E2BA), 2023.
- 752 Schumann, U. and Huntrieser, H.: The global lightning-induced nitrogen oxides source, *Atmos. Chem. Phys*, 7, 3823–3907,  
753 2007.
- 754 Seo, S., Kim, S. W., Kim, K. M., Lamsal, L. N., and Jin, H.: Reductions in NO<sub>2</sub> concentrations in Seoul, South Korea detected  
755 from space and ground-based monitors prior to and during the COVID-19 pandemic, *Environ Res Commun*, 3, 051005,  
756 <https://doi.org/10.1088/2515-7620/ABED92>, 2021.
- 757 Shi, Q., Zheng, B., Zheng, Y., Tong, D., Liu, Y., Ma, H., Hong, C., Geng, G., Guan, D., He, K., and Zhang, Q.: Co-benefits  
758 of CO<sub>2</sub> emission reduction from China's clean air actions between 2013-2020, *Nature Communications* 2022 13:1, 13, 1–  
759 8, <https://doi.org/10.1038/s41467-022-32656-8>, 2022.
- 760 Shikwambana, L., Mhangara, P., and Mbatha, N.: Trend analysis and first time observations of sulphur dioxide and nitrogen  
761 dioxide in South Africa using TROPOMI/Sentinel-5 P data, *International Journal of Applied Earth Observation and*  
762 *Geoinformation*, 91, 102130, <https://doi.org/10.1016/J.JAG.2020.102130>, 2020.
- 763 Song, W., Liu, X. Y., Hu, C. C., Chen, G. Y., Liu, X. J., Walters, W. W., Michalski, G., and Liu, C. Q.: Important contributions  
764 of non-fossil fuel nitrogen oxides emissions, *Nature Communications* 2021 12:1, 12, 1–7, [https://doi.org/10.1038/s41467-](https://doi.org/10.1038/s41467-020-20356-0)  
765 [020-20356-0](https://doi.org/10.1038/s41467-020-20356-0), 2021.
- 766 Stavrakou, T., Müller, J.-F., Boersma, K. F., De Smedt, I., and van der A, R. J.: Assessing the distribution and growth rates of  
767 NO<sub>x</sub> emission sources by inverting a 10-year record of NO<sub>2</sub> satellite columns, *Geophys Res Lett*, 35,  
768 <https://doi.org/10.1029/2008GL033521>, 2008.
- 769 VanDerA, R. J., Eskes, H. J., Boersma, K. F., van Noije, T. P. C., Van Roozendaal, M., De Smedt, I., Peters, D. H. M. U., and  
770 Meijer, E. W.: Trends, seasonal variability and dominant NO<sub>x</sub> source derived from a ten year record of NO<sub>2</sub> measured  
771 from space, *Journal of Geophysical Research Atmospheres*, 113, 1–12, <https://doi.org/10.1029/2007JD009021>, 2008.
- 772 Varma, A. K., Biswal, S., Hazra, B., Mendhe, V. A., Misra, S., Samad, S. K., Singh, B. D., Dayal, A. M., and Mani, D.:  
773 Petrographic characteristics and methane sorption dynamics of coal and shaly-coal samples from Ib Valley Basin, Odisha,  
774 India, *Int J Coal Geol*, 141–142, 51–62, <https://doi.org/10.1016/J.COAL.2015.03.005>, 2015.
- 775 Veefkind, J. P., Aben, I., McMullan, K., Förster, H., de Vries, J., Otter, G., Claas, J., Eskes, H. J., de Haan, J. F., Kleipool, Q.,  
776 van Weele, M., Hasekamp, O., Hoogeveen, R., Landgraf, J., Snel, R., Tol, P., Ingmann, P., Voors, R., Kruizinga, B., Vink,  
777 R., Visser, H., and Levelt, P. F.: TROPOMI on the ESA Sentinel-5 Precursor: A GMES mission for global observations

778 of the atmospheric composition for climate, air quality and ozone layer applications, *Remote Sens Environ*, 120, 70–83,  
779 <https://doi.org/10.1016/J.RSE.2011.09.027>, 2012.

780 Vlemmix, T., PETERS, A. J. M., STAMMES, P., WANG, P., and LEVELT, P. F.: Retrieval of tropospheric NO<sub>2</sub> using the MAX-DOAS  
781 method combined with relative intensity measurements for aerosol correction, *Atmos Meas Tech*, 3, 1287–1305,  
782 <https://doi.org/10.5194/AMT-3-1287-2010>, 2010.

783 Wang, C., Wang, T., and Wang, P.: The Spatial–Temporal Variation of Tropospheric NO<sub>2</sub> over China during 2005 to 2018,  
784 *Atmosphere* 2019, Vol. 10, Page 444, 10, 444, <https://doi.org/10.3390/ATMOS10080444>, 2019.

785 Zhang, Y., Tian, J., Feng, S., Yang, F., and Lu, X.: The occurrence modes and geologic origins of arsenic in coal from  
786 Santanghu Coalfield, Xinjiang, *J Geochem Explor*, 186, 225–234, <https://doi.org/10.1016/J.GEXPLO.2017.12.006>, 2018.

787 Zhao, X., Li, X. X., Xin, R., Zhang, Y., and Liu, C. H.: Impact of Lockdowns on Air Pollution: Case Studies of Two Periods  
788 in 2022 in Guangzhou, China, *Atmosphere* 2024, Vol. 15, Page 1144, 15, 1144,  
789 <https://doi.org/10.3390/ATMOS15091144>, 2024.

790 Zheng, B., Zhang, Q., Geng, G., Chen, C., Shi, Q., Cui, M., Lei, Y., and He, K.: Changes in China’s anthropogenic emissions  
791 and air quality during the COVID-19 pandemic in 2020, *Earth Syst Sci Data*, 13, 2895–2907,  
792 <https://doi.org/10.5194/ESSD-13-2895-2021>, 2021.

793